Position Estimation via a Single LEO Satellite based on Pseudorange and Doppler Measurements

KAMIL ANIL ISIK, Student Member, IEEE
Department of Electrical and Electronics Engineering, Bilkent University, Ankara 06800, Türkiye

SINAN GEZICI, Fellow, IEEE
Department of Electrical and Electronics Engineering, Bilkent University, Ankara 06800, Türkiye

***Abstract*— We focus on the problem of positioning a stationary ground receiver using measurements from a single Low Earth Orbit (LEO) satellite. A joint observation model based on pseudorange and pseudorange rate (Doppler) measurements is employed, which explicitly accounts for correlations between measurement noise components in a given time epoch. The exact maximum likelihood estimator (MLE) for the receiver position, clock bias, and clock drift is derived, and it is shown that the original five-dimensional estimation problem can be reduced to a three-dimensional position search by analytically eliminating the clock parameters without loss of optimality. In addition, closed form expressions for the Cramér–Rao lower bound (CRLB) are obtained, providing fundamental performance limits for single LEO positioning with joint measurements. The analysis is further extended to scenarios in which the satellite state is known only at reception times by incorporating the propagation delay effect through an explicit time of flight model. Numerical simulations using realistic LEO orbital parameters demonstrate the impact of noise level, sampling time, receiver-orbital plane angle, and measurement noise correlation on positioning accuracy by presenting the performance of the MLE together with the CRLB. Moreover, the proposed MLE approach is compared against the Doppler-only, pseudorange-only, and correlation-ignorant MLEs.**

***Index Terms*— CRLB, Doppler, estimation, LEO satellite, positioning, pseudorange.**

I. INTRODUCTION

In recent years, low Earth orbit (LEO) satellite constellations have attracted significant attention due to the rapid deployment of large-scale satellite networks and advances in communication and signal processing technologies. While these systems are primarily designed for broadband communication services, their integration with emerging 5G/6G networks and Internet of Things (IoT) ecosystems has opened new opportunities for global connectivity and remote sensing [1], [2], [3]. Although the primary function of LEO satellites is communication, they possess several characteristics that make them highly attractive for opportunistic navigation and positioning applications [4], [5] [6].

LEO satellite systems have several desirable properties for positioning. Operating at significantly lower orbital altitudes than Medium Earth Orbit (MEO) Global Navigation Satellite System (GNSS) satellites, LEO satellites provide received signal power levels that are approximately 30 dB stronger, which enhances signal availability in challenged and GNSS-denied environments [4], [7]. In addition, the high orbital velocity of LEO satellites relative to ground receivers results in rapidly time varying Doppler shifts, offering rich Doppler observability that can be utilized for positioning, even under limited satellite visibility conditions [7], [8], [9], [10], [11], [12]. Furthermore, the emergence of large scale LEO constellations such as Starlink, OneWeb, and Kuiper provides a diverse set of signal sources with high geometric and spectral density, which further motivates their use as signals of opportunity (SOOP) for positioning [11], [13], [14], [15], [16].

Despite these favorable signal and system properties, LEO satellites generally lack key features that characterize GNSS systems for navigation purposes, including highly stable onboard atomic clocks, and precise and continuously broadcast ephemeris parameters [17], [18], [19]. As a result, LEO satellite state information may be subject to significant uncertainties compared to GNSS satellites. This limitation has motivated the development of estimation frameworks that rely on receiver-side processing to jointly estimate receiver and satellite related parameters, or to perform joint orbit determination [17], [20], [21]. A range of estimation frameworks for positioning using LEO satellite systems has been examined in the literature [7], [11], [14], [22], [23], [24], [25], [26]. These approaches can broadly be categorized into two classes. The first class considers LEO aided positioning frameworks, in which LEO satellite measurements are integrated with complementary sensors or systems, such as inertial measurement units (IMUs) or GNSS. The second class focuses on standalone LEO-based positioning, which includes Doppler only techniques, joint Doppler pseudorange processing, multiple configuration signal analysis, and single satellite localization scenarios. Overall, these studies establish the feasibility of LEO signals of opportunity as a source for positioning.

In the first class, the integration of LEO satellite measurements with inertial sensing is investigated to support navigation in GNSS denied environments. In these studies, Doppler or Doppler related measurements based on LEO satellite signals are tightly coupled with inertial measurements from an IMU, typically consisting of gyroscopes and accelerometers, and in some cases augmented

Kamil Anil Isik and Sinan Gezici are with the Department of Electrical and Electronics Engineering, Bilkent University, Ankara 06800, Türkiye (e-mail: anil.isik@bilkent.edu.tr; gezici@ee.bilkent.edu.tr). *(Corresponding author: S. Gezici.)*

with magnetometer measurements to enhance attitude and orientation observability [23], [27], [28]. Such integration is commonly performed with extended Kalman filter (EKF) frameworks that jointly estimate position, velocity, attitude, inertial sensor biases, and clock states while explicitly accounting for asynchronous satellite clocks and ephemeris uncertainties [29], [30]. In addition to LEO-IMU integration, some studies consider tightly coupled GNSS-LEO integration, in which GNSS pseudorange and Doppler measurements are jointly processed with LEO Doppler or pseudorange rate measurements while explicitly modeling system clock offsets and drifts, leading to improved vertical positioning performance [8], [31]. Other works focus on aiding GNSS positioning with LEO Doppler measurements within weighted least squares or Kalman filtering frameworks [1], [32], [33]. Moreover, LEO-enhanced GNSS (LeGNSS) architectures are proposed to accelerate precise point positioning (PPP) convergence by leveraging the fast changing geometry of LEO satellites [34], [35].

The second class focuses on standalone LEO-based positioning, where receiver localization is achieved based on measurements derived only from LEO satellite signals without depending on external auxiliary sensors or systems. Within this class, Doppler only positioning techniques utilize the strong Doppler dynamics due to the high relative velocity of LEO satellites to estimate receiver states [7], [36]. While such approaches establish the opportunity for LEO-based localization, they typically require long observation intervals or the availability of multiple satellites to sufficiently resolve position ambiguities. To improve estimation accuracy and robustness, other studies incorporate pseudorange measurements alongside Doppler related measurements, showing that joint pseudorange and Doppler processing can improve geometric conditioning and positioning performance compared to Doppler only methods [11]. In addition, multi-constellation frameworks using heterogeneous LEO systems have been investigated to enhance solution availability and reduce system uncertainties [13], [14], [23], [22]. Moreover, in recent years, positioning with a single LEO satellite rather than constellations has drawn attention due to its opportunity to lower cost and improve flexibility. Although positioning with multiple LEO satellites can potentially improve geometric diversity and accuracy, it requires the receiver to acquire and track multiple satellite signals simultaneously, which increases the receiver cost and complexity. Also, in some scenarios, visibility of LEO satellites can be low due to partial sky blockage, low-elevation masks, or temporary constellation sparsity, where positioning via single LEO satellite can be the only option. Therefore, for simple receiver structures and low satellite visibility, single-satellite positioning provides operational flexibility in position estimation. To characterize the potential of positioning via a single LEO satellite, theoretical accuracy bounds have been characterized through Cramér–Rao lower bound (CRLB) analyses [24], [25], [37]. Joint Doppler and pseudorange measurements have been explored to improve single LEO localization accuracy, with estimator performance evaluated against CRLB bounds under simplifying assumptions regarding noise distributions [25]. Observability analyses have also been conducted to determine the conditions under which a receiver state can be recovered from pseudorange measurements from a single LEO satellite [9].

While previous studies have demonstrated that single-LEO satellite positioning is feasible and promising, important aspects of this problem still require further investigation. In particular, prior works have considered different measurement configurations, including Doppler-only positioning [7], pseudorange-only localization [9], Doppler-aided formulations [26], and joint Doppler and pseudorange based positioning [25]. However, existing joint pseudorange and Doppler formulations for single-LEO positioning typically rely on simplified measurement noise assumptions and do not explicitly account for the statistical dependence between the pseudorange and pseudorange-rate measurement errors within the same time epoch. Therefore, the impact of such same-epoch noise correlation on both estimator design and achievable positioning accuracy remains unclear.

In this manuscript, we propose a theoretical framework for positioning a stationary ground receiver using both pseudorange and Doppler measurements from a single LEO satellite. We formulate the exact maximum likelihood estimator (MLE) and derive the corresponding CRLB for the joint estimation problem. While the considered problem setting is similar to the single LEO positioning framework studied in [25], our work presents an extensive analysis by (i) explicitly incorporating correlated measurement noises into the system model, (ii) deriving explicit MLE and CRLB expressions, and (iii) addressing the propagation delay effect [38], in which the satellite state is known at reception times rather than at transmission times. Since time delay estimation and carrier frequency estimation can be performed based on the same signals in a given time epoch, pseudorange and Doppler measurements can be correlated in practical systems. Hence, consideration of correlated measurements can be crucial for accurate estimation of receiver position. The main contributions of our study can be summarized as follows:

- By explicitly accounting for correlations between measurement noises within a given time epoch, we formulate the position estimation problem for a stationary ground receiver using a single LEO satellite via a joint observation model based on pseudorange and pseudorange-rate (Doppler) measurements.
- We obtain the MLE for the proposed problem and derive an exact and low-complexity implementation that reduces the 5-dimensional search space (over position, clock bias and clock drift parameters) into a 3-dimensional position search by analytically solving for the clock parameters.

- We derive a new CRLB expression for joint pseudorange and pseudorange-rate measurements in the presence of correlated noise components in given time epochs, which is used as a theoretical performance benchmark, quantifying the impact of measurement quality and satellite geometry.
- We evaluate the MLE performance and compare it against the CRLB on positioning via numerical simulations using realistic orbital parameters and considering various factors such as receiver-orbital plane angle, sampling interval, range measurement noise variance, Doppler measurement noise variance, and measurement noise correlation.
- We conduct benchmark comparisons of the proposed MLE method against pseudorange-only, pseudorange-rate (Doppler)-only, and correlation-ignorant MLE formulations.
- We extend our study to account for the propagation delay effect, dealing with scenarios where satellite state is known at reception times rather than at transmission times.

The remainder of the manuscript is organized as follows. Section II introduces the system model along with the pseudorange and Doppler measurement equations. The proposed estimation framework and the derivation of the MLE and the CRLB are presented in Section III. Section IV reports simulation results, compares the performance of the MLE with the derived performance bounds, and presents benchmark comparisons with pseudorange-only, pseudorange-rate (Doppler)-only, and correlation-ignorant MLE formulations. The extension of the proposed estimation framework considering propagation delay effects is discussed in Section V. Finally, concluding remarks are provided in Section VI.

II. System Model

We consider a ground receiver that takes a number of pseudorange and Doppler measurements from a single LEO satellite in a certain time interval. The aim is to estimate the three-dimensional position of the receiver based on these measurements by taking into account the unknown clock bias and clock drift parameters for the receiver.

Let $\boldsymbol{r}_{\rm rx}(k) \in \mathbb{R}^3$ denote the position of the receiver at discrete time index k, which corresponds to a time instant of $t_k = kT + t_0$, with T denoting the period for taking measurements and t_0 being an initial time instant [39]. Also, $\boldsymbol{r}_{\rm leo}(k') \in \mathbb{R}^3$ represents the position of the LEO satellite at time index k' that is given by $t_{k'} = t_k - \delta t_{\rm TOF}(k)$, where $\delta t_{\rm TOF}(k)$ is the true time-of-flight of the signal from the satellite to the receiver. The time index k and the time index k' correspond to *reception time* and *transmission time*, respectively [38]. That is, the satellite transmits a signal at time $t_{k'}$ and it reaches the receiver at time t_k. The receiver collects $N_{\rm M} \geq 2$ pseudorange measurements denoted by $\{\rho(k)\}_{k=1}^{N_{\rm M}}$ and $N_{\rm M} \geq 2$ pseudorange rate measurements (obtained from Doppler measurements) represented by $\{\dot\rho(k)\}_{k=1}^{N_{\rm M}}$, which are described in the following [39].

After mitigation of ionospheric and tropospheric delays [39], the pseudorange measurement at discrete time index k (that is, at time $t_k = kT + t_0$) is modeled as

$$\rho(k) = \|\boldsymbol{r}_{\rm rx}(k) - \boldsymbol{r}_{\rm leo}(k')\| + c\,(\delta t_{\rm rx}(k) - \delta t_{\rm leo}(k')) + v_\rho(k), \tag{1}$$

for $k = 1, \ldots, N_{\rm M}$, where $\delta t_{\rm rx}(k)$ and $\delta t_{\rm leo}(k')$ are the clock biases of the receiver and the LEO satellite, respectively, c is the speed of light, and $v_\rho(k)$ is measurement noise modeled as a zero mean Gaussian random variable with variance σ_k^2 that is independent of $v_\rho(l)$ for all $l \neq k$.

On the other hand, the pseudorange rate measurement (which is obtained from the Doppler measurement by scaling it with $-c/f_c$, where c is the speed of light and f_c is the carrier frequency) at discrete time k is given by [39]

$$\begin{aligned}\dot\rho(k) = &\frac{(\dot{\boldsymbol{r}}_{\rm rx}(k) - \dot{\boldsymbol{r}}_{\rm leo}(k'))^T(\boldsymbol{r}_{\rm rx}(k) - \boldsymbol{r}_{\rm leo}(k'))}{\|\boldsymbol{r}_{\rm rx}(k) - \boldsymbol{r}_{\rm leo}(k')\|} \\ &+ c\big(\dot{\delta t}_{\rm rx}(k) - \dot{\delta t}_{\rm leo}(k')\big) + v_{\dot\rho}(k),\end{aligned} \tag{2}$$

for $k = 1, \ldots, N_{\rm M}$, where $\dot{\boldsymbol{r}}_{\rm rx}(k)$ and $\dot{\boldsymbol{r}}_{\rm leo}(k')$ are the velocity vectors of the receiver and the LEO satellite, respectively, $\dot{\delta t}_{\rm rx}(k)$ and $\dot{\delta t}_{\rm leo}(k')$ are the clock drifts of the receiver and the LEO satellite, respectively, and $v_{\dot\rho}(k)$ is zero-mean Gaussian noise with variance $\tilde\sigma_k^2$, which is independent of $v_{\dot\rho}(l)$ for all $l \neq k$.

The aim is to estimate the position of the receiver based on the pseudorange and pseudorange rate measurements as modeled above under the following assumptions:

(A1) During the measurements, the receiver is stationary.[1] That is, $\boldsymbol{r}_{\rm rx}(k) = \boldsymbol{r}_{\rm rx}$ and $\dot{\boldsymbol{r}}_{\rm rx}(k) = \boldsymbol{0}$ for all $k = 1, \ldots, N_{\rm M}$.

(A2) The unknown parameters (state) of the satellite are known at each transmission time [9]. Namely, the position, velocity vector, and clock errors (clock bias and drift) of the satellite are assumed to be known at each transmission time instant.[2] For example, some satellites, such as Orbcomm, transmit their ephemeris and clock errors, which are estimated via onboard GPS receivers, in their communication packets [39].

(A3) The receiver clock operates according to the following affine model [15], [40]:

$$\delta t_{\rm rx}(t) = b + d(t - t_0), \tag{3}$$

where b specifies the clock bias (offset) and d is the clock drift ("skew"). Therefore, the $\delta t_{\rm rx}(k)$ and $\dot{\delta t}_{\rm rx}(k)$ terms in (1) and (2) can be stated from (3) as

$$\delta t_{\rm rx}(k) = b + kTd, \tag{4}$$

$$\dot{\delta t}_{\rm rx}(k) = d. \tag{5}$$

[1]Extensions are possible when the receiver moves with a known velocity vector so that it can determine its relative position at each time instant.

[2]The results will be extended to cases in which the satellite state is known at each reception time in Section V.

Based on these assumptions, the measurements in (1) and (2) can be specified as follows:

$$\rho(k) = \|\boldsymbol{r}_{\rm rx} - \boldsymbol{r}_{\rm leo}(k')\| + c(b + kTd - \delta t_{\rm leo}(k')) + v_\rho(k), \tag{6}$$

$$\dot{\rho}(k) = \frac{-\dot{\boldsymbol{r}}_{\rm leo}(k')^T(\boldsymbol{r}_{\rm rx} - \boldsymbol{r}_{\rm leo}(k'))}{\|\boldsymbol{r}_{\rm rx} - \boldsymbol{r}_{\rm leo}(k')\|} + c(d - \dot{\delta t}_{\rm leo}(k')) + v_{\dot\rho}(k), \tag{7}$$

for $k = 1, \ldots, N_{\rm M}$, where $\boldsymbol{r}_{\rm leo}(k')$, $\dot{\boldsymbol{r}}_{\rm leo}(k')$, $\delta t_{\rm leo}(k')$, and $\dot{\delta t}_{\rm leo}(k')$ are known for all indices due to Assumption 2.

Remark 1: In practice, the parameters of the satellite may not be known perfectly since reported ephemeris and clock errors can be inaccurate or there can be estimation errors while determining these parameters. Therefore, our analysis based on Assumption 2 provides a lower bound on estimation accuracy of receiver position in this ideal scenario. In future work, a misspecified estimation framework can be utilized to analyze the effects of inaccuracies about the satellite parameters based on the misspecified Cramér–Rao bound (MCRB) [41], [42], [43]. ■

III. Position Estimation

Based on the pseudorange and pseudorange rate measurements in (6) and (7), the aim is to estimate the 5-dimensional unknown parameter vector $\boldsymbol{\theta}$ specified as

$$\boldsymbol{\theta} = \left[\boldsymbol{r}_{\rm rx}^T, b, d\right]^T \tag{8}$$

where $\boldsymbol{r}_{\rm rx}$ is the 3-dimensional position of the receiver, and b and d are, respectively, the clock bias and the clock drift parameters of the receiver, which can be considered as nuisance parameters.

A. Likelihood Function

To derive the MLE and the CRLB, the first step is to obtain the likelihood function for parameter $\boldsymbol{\theta}$ in (8) based on the measurements in (6) and (7). We collect these measurement into a measurement (observation) vector as follows:

$$\boldsymbol{y} \triangleq [\rho(1), \dot\rho(1), \ldots, \rho(N_{\rm M}), \dot\rho(N_{\rm M})]^T. \tag{9}$$

Although the measurement noise components in pseudorange and pseudorange rate measurements in (9) can be modeled as independent random variables for different time epochs, they can be correlated for the same time epochs. (Time delay estimation and carrier frequency estimation can be performed based on the same signals, leading to correlations between pseudorange and Doppler measurements/estimates.) Therefore, we consider the correlation between such measurement noise components and model the overall measurement noise vector, denoted by $\boldsymbol{v}$, as a multivariate Gaussian random vector as follows:

$$\boldsymbol{v} \triangleq [v_\rho(1), v_{\dot\rho}(1), \ldots, v_\rho(N_{\rm M}), v_{\dot\rho}(N_{\rm M})]^T \sim \mathcal{N}(\boldsymbol{0}, \boldsymbol{\Sigma}_v) \tag{10}$$

where $\{v_\rho(k)\}_{k=1}^{N_{\rm M}}$ and $\{v_{\dot\rho}(k)\}_{k=1}^{N_{\rm M}}$ are as defined in (6) and (7), and

$$\boldsymbol{\Sigma}_v = {\rm diag}\{\mathbf{R}_1, \ldots, \mathbf{R}_{N_{\rm M}}\} \tag{11}$$

with

$$\mathbf{R}_k = \begin{bmatrix} \sigma_k^2 & \gamma_k \\ \gamma_k & \tilde\sigma_k^2 \end{bmatrix} \tag{12}$$

for $k = 1, \ldots, N_{\rm M}$. Here, γ_k denotes the covariance between $v_\rho(k)$ and $v_{\dot\rho}(k)$, and $\mathbf{R}_k$ is assumed to be positive definite for each k.

From (6), (7), and (10), we can express the measurement vector in (9) as

$$\boldsymbol{y} = \boldsymbol{h}(\boldsymbol{\theta}) + \boldsymbol{v}, \tag{13}$$

where

$$\boldsymbol{h}(\boldsymbol{\theta}) \triangleq [\mu_\rho(1;\boldsymbol{\theta}),\, \mu_{\dot\rho}(1;\boldsymbol{\theta}),\, \ldots,\, \mu_\rho(N_{\rm M};\boldsymbol{\theta}),\, \mu_{\dot\rho}(N_{\rm M};\boldsymbol{\theta})]^T, \tag{14}$$

with

$$\mu_\rho(k;\boldsymbol{\theta}) \triangleq \|\boldsymbol{r}_{\rm rx} - \boldsymbol{r}_{\rm leo}(k')\| + c(b + kTd - \delta t_{\rm leo}(k')), \tag{15}$$

$$\mu_{\dot\rho}(k;\boldsymbol{\theta}) \triangleq \frac{-\dot{\boldsymbol{r}}_{\rm leo}(k')^T(\boldsymbol{r}_{\rm rx} - \boldsymbol{r}_{\rm leo}(k'))}{\|\boldsymbol{r}_{\rm rx} - \boldsymbol{r}_{\rm leo}(k')\|} + c(d - \dot{\delta t}_{\rm leo}(k')). \tag{16}$$

Based on the measurement vector in (13) and the multivariate Gaussian noise model specified in (10)–(12), the log-likelihood function for parameter $\boldsymbol{\theta}$ can be derived as

$$\log p(\boldsymbol{y}|\boldsymbol{\theta}) = -\frac{1}{2}\big(\boldsymbol{y} - \boldsymbol{h}(\boldsymbol{\theta})\big)^T \boldsymbol{\Sigma}_v^{-1}\big(\boldsymbol{y} - \boldsymbol{h}(\boldsymbol{\theta})\big) - \frac{1}{2}\log(\det \boldsymbol{\Sigma}_v) - N_{\rm M}\log(2\pi). \tag{17}$$

To obtain an explicit expression for this log-likelihood function, we define the following residual terms for each time epoch:

$$e_\rho(k;\boldsymbol{\theta}) \triangleq \rho(k) - \mu_\rho(k;\boldsymbol{\theta}), \tag{18}$$

$$e_{\dot\rho}(k;\boldsymbol{\theta}) \triangleq \dot\rho(k) - \mu_{\dot\rho}(k;\boldsymbol{\theta}). \tag{19}$$

In addition, the inverse of $\mathbf{R}_k$ in (12) is obtained as

$$\mathbf{R}_k^{-1} = \frac{1}{\sigma_k^2\tilde\sigma_k^2 - \gamma_k^2}\begin{bmatrix} \tilde\sigma_k^2 & -\gamma_k \\ -\gamma_k & \sigma_k^2 \end{bmatrix}. \tag{20}$$

Consequently, an explicit expression for (17) can be obtained as

$$\log p(\boldsymbol{y}|\boldsymbol{\theta}) = -\frac{1}{2}\sum_{k=1}^{N_{\rm M}} \frac{\tilde\sigma_k^2 e_\rho(k;\boldsymbol{\theta})^2 - 2\gamma_k e_\rho(k;\boldsymbol{\theta}) e_{\dot\rho}(k;\boldsymbol{\theta}) + \sigma_k^2 e_{\dot\rho}(k;\boldsymbol{\theta})^2}{\sigma_k^2\tilde\sigma_k^2 - \gamma_k^2} - \frac{1}{2}\sum_{k=1}^{N_{\rm M}} \log(\sigma_k^2\tilde\sigma_k^2 - \gamma_k^2) - N_{\rm M}\log(2\pi). \tag{21}$$

B. Maximum Likelihood Estimator (MLE)

From (21), the MLE for the unknown parameter vector $\boldsymbol{\theta}$ can be stated as follows:

$$\hat{\boldsymbol{\theta}}_{\mathrm{mle}}(\boldsymbol{y}) = \arg\min_{\boldsymbol{\theta}\in\mathcal{S}} \sum_{k=1}^{N_{\mathrm{M}}} \frac{\tilde{\sigma}_k^2 e_\rho(k;\boldsymbol{\theta})^2 - 2\gamma_k e_\rho(k;\boldsymbol{\theta}) e_{\dot\rho}(k;\boldsymbol{\theta}) + \sigma_k^2 e_{\dot\rho}(k;\boldsymbol{\theta})^2}{\sigma_k^2\tilde{\sigma}_k^2 - \gamma_k^2} \tag{22}$$

where $\mathcal{S} \subset \mathbb{R}^5$ denotes the set of possible values for $\boldsymbol{\theta}$, and $e_\rho(k;\boldsymbol{\theta})$ and $e_{\dot\rho}(k;\boldsymbol{\theta})$ are as defined in (18) and (19). The MLE in (22) performs joint estimation of the receiver position, and the clock bias and clock drift of the receiver, which calls for a 5-dimensional search. However, as stated in the following lemma, the solution of (22) can be obtained with a 3-dimensional search without any loss of optimality.

Lemma 1: *The MLE for the receiver position can be obtained as follows:*

$$\hat{\boldsymbol{r}}_{\mathrm{rx}}^{\mathrm{mle}}(\boldsymbol{y}) = \arg\min_{\boldsymbol{r}_{\mathrm{rx}}\in\mathcal{S}_{\mathrm{rx}}} \sum_{k=1}^{N_{\mathrm{M}}} \frac{1}{\sigma_k^2\tilde{\sigma}_k^2 - \gamma_k^2} \times \Bigg(\tilde{\sigma}_k^2 \left(f_k(\boldsymbol{r}_{\mathrm{rx}}) - c\hat{b}(\boldsymbol{r}_{\mathrm{rx}}) - kcT\hat{d}(\boldsymbol{r}_{\mathrm{rx}}) \right)^2 - 2\gamma_k \left(f_k(\boldsymbol{r}_{\mathrm{rx}}) - c\hat{b}(\boldsymbol{r}_{\mathrm{rx}}) - kcT\hat{d}(\boldsymbol{r}_{\mathrm{rx}}) \right) \left(g_k(\boldsymbol{r}_{\mathrm{rx}}) - c\hat{d}(\boldsymbol{r}_{\mathrm{rx}}) \right) + \sigma_k^2 \left(g_k(\boldsymbol{r}_{\mathrm{rx}}) - c\hat{d}(\boldsymbol{r}_{\mathrm{rx}}) \right)^2 \Bigg) \tag{23}$$

where $\mathcal{S}_{\mathrm{rx}} \subset \mathbb{R}^3$ represents the set of possible positions for the receiver,

$$f_k(\boldsymbol{r}_{\mathrm{rx}}) \triangleq \rho(k) - \|\boldsymbol{r}_{\mathrm{rx}} - \boldsymbol{r}_{\mathrm{leo}}(k')\| + c\delta t_{\mathrm{leo}}(k'), \tag{24}$$

$$g_k(\boldsymbol{r}_{\mathrm{rx}}) \triangleq \dot\rho(k) + \frac{\dot{\boldsymbol{r}}_{\mathrm{leo}}(k')^T(\boldsymbol{r}_{\mathrm{rx}} - \boldsymbol{r}_{\mathrm{leo}}(k'))}{\|\boldsymbol{r}_{\mathrm{rx}} - \boldsymbol{r}_{\mathrm{leo}}(k')\|} + c\dot{\delta t}_{\mathrm{leo}}(k'), \tag{25}$$

and $\hat{b}(\boldsymbol{r}_{\mathrm{rx}})$ and $\hat{d}(\boldsymbol{r}_{\mathrm{rx}})$ are, respectively, the MLEs of the clock bias and clock drift of the receiver for a given receiver position, which are calculated as

$$\begin{bmatrix} \hat{b}(\boldsymbol{r}_{\mathrm{rx}}) \\ \hat{d}(\boldsymbol{r}_{\mathrm{rx}}) \end{bmatrix} = \frac{1}{\alpha_1\beta_2 - \alpha_2^2} \begin{bmatrix} \alpha_0\beta_2 - \alpha_2\beta_0 \\ \alpha_1\beta_0 - \alpha_0\alpha_2 \end{bmatrix} \tag{26}$$

with

$$\alpha_0 \triangleq \sum_{k=1}^{N_{\mathrm{M}}} \frac{\tilde{\sigma}_k^2 f_k(\boldsymbol{r}_{\mathrm{rx}}) - \gamma_k g_k(\boldsymbol{r}_{\mathrm{rx}})}{\sigma_k^2\tilde{\sigma}_k^2 - \gamma_k^2}, \tag{27}$$

$$\alpha_1 \triangleq c \sum_{k=1}^{N_{\mathrm{M}}} \frac{\tilde{\sigma}_k^2}{\sigma_k^2\tilde{\sigma}_k^2 - \gamma_k^2}, \tag{28}$$

$$\alpha_2 \triangleq c \sum_{k=1}^{N_{\mathrm{M}}} \frac{kT\tilde{\sigma}_k^2 - \gamma_k}{\sigma_k^2\tilde{\sigma}_k^2 - \gamma_k^2}, \tag{29}$$

$$\beta_0 \triangleq \sum_{k=1}^{N_{\mathrm{M}}} \frac{f_k(\boldsymbol{r}_{\mathrm{rx}})(\tilde{\sigma}_k^2 kT - \gamma_k) + g_k(\boldsymbol{r}_{\mathrm{rx}})(\sigma_k^2 - \gamma_k kT)}{\sigma_k^2\tilde{\sigma}_k^2 - \gamma_k^2}, \tag{30}$$

$$\beta_2 \triangleq c \sum_{k=1}^{N_{\mathrm{M}}} \frac{\tilde{\sigma}_k^2 (kT)^2 - 2\gamma_k kT + \sigma_k^2}{\sigma_k^2\tilde{\sigma}_k^2 - \gamma_k^2}. \tag{31}$$

Proof: Based on the definitions in (15), (16), (24) and (25), the $e_\rho(k;\boldsymbol{\theta})$ and $e_{\dot\rho}(k;\boldsymbol{\theta})$ terms in (18) and (19) can be expressed as

$$e_\rho(k;\boldsymbol{\theta}) = f_k(\boldsymbol{r}_{\mathrm{rx}}) - cb - kcTd, \tag{32}$$

$$e_{\dot\rho}(k;\boldsymbol{\theta}) = g_k(\boldsymbol{r}_{\mathrm{rx}}) - cd. \tag{33}$$

Therefore, the objective function in (22) becomes

$$\sum_{k=1}^{N_{\mathrm{M}}} \frac{1}{\sigma_k^2\tilde{\sigma}_k^2 - \gamma_k^2} \Big(\tilde{\sigma}_k^2 (f_k(\boldsymbol{r}_{\mathrm{rx}}) - cb - kcTd)^2 - 2\gamma_k \times (f_k(\boldsymbol{r}_{\mathrm{rx}}) - cb - kcTd)(g_k(\boldsymbol{r}_{\mathrm{rx}}) - cd) + \sigma_k^2 (g_k(\boldsymbol{r}_{\mathrm{rx}}) - cd)^2 \Big) \tag{34}$$

By taking the partial derivatives of the objective function in (34) with respect to b and d, and equating them to zero yields the following, after some manipulation:

$$\alpha_0 - b\alpha_1 - d\alpha_2 = 0, \tag{35}$$

$$\beta_0 - b\alpha_2 - d\beta_2 = 0, \tag{36}$$

where α_0, α_1, α_2, β_0, and β_2 are as in (27)–(31).[3] The solution of (35) and (36) can be obtained as in (26), which corresponds to the MLEs for b and d for a given value of $\boldsymbol{r}_{\mathrm{rx}}$, denoted by $\hat{b}(\boldsymbol{r}_{\mathrm{rx}})$ and $\hat{d}(\boldsymbol{r}_{\mathrm{rx}})$. Therefore, we insert the MLEs for b and d (i.e., $\hat{b}(\boldsymbol{r}_{\mathrm{rx}})$ and $\hat{d}(\boldsymbol{r}_{\mathrm{rx}})$) into (34), and minimize it over $\boldsymbol{r}_{\mathrm{rx}}$, which results in (23). Hence, the solution of (22) can be obtained exactly via (23) and (26) in a low-complexity manner. ■

Lemma 1 provides a low-complexity approach to ML estimation for the receiver position, which corresponds to the *exact* solution of the 5-dimensional search formulation in (22). Namely, by performing a 3-dimensional search as in (23) and utilizing the closed form solution for the MLEs of the clock bias and clock drift parameters for each receiver position ((26)–(31)), the MLE for the receiver position is obtained in a low-complexity manner, together with the MLEs for the clock bias and the clock drift parameters.

Remark 2: Although Lemma 1 reduces the MLE problem from 5 dimensions to 3 dimensions, the resulting objective function is still non-convex with multiple local minima in general. Therefore, we apply a two-step approach to solve it by first performing a coarse grid search and then running an iterative algorithm (Levenberg–Marquardt) initialized with the result of the grid search. As the grid search dominates the computational complexity in general, the proposed reduction to 3 dimensions can still provide significant complexity reduction compared to the original 5-dimensional problem. In addition, for the iterative algorithm in the second step, the MLE formulation in Lemma 1 facilitates faster convergence as it provides a lower-dimensional objective function. ■

[3]It can be shown that the objective function in (34) is a strictly convex quadratic function of (b, d) provided that $N_{\mathrm{M}} \geq 2$ and $\sigma_k^2\tilde{\sigma}_k^2 - \gamma_k^2 > 0$ for all $k = 1, \ldots, N_{\mathrm{M}}$. Hence, setting the first order partial derivatives to zero yields a unique minimizer for the clock bias and the clock drift parameters.

C. Cramér-Rao Lower Bound (CRLB)

CRLB provides a lower limit on MSEs of unbiased estimators, which can be calculated from the likelihood function without considering a specific estimator structure [44]. The MLE is known to be asymptotically efficient (under some mild regularity conditions), meaning that its MSE converges to the CRLB asymptotically [44]. Therefore, CRLB can provide a useful and practical bound to analyze positioning accuracy of LEO positioning systems.

Based on the log-likelihood function in (21), the CRLB for estimating the receiver position based on the measurements in $\boldsymbol{y}$ in (9) can be specified as in the following lemma.

Lemma 2: *The CRLB on the estimation of the receiver position $\boldsymbol{r}_{\rm rx}$ from the pseudorange and pseudorange rate measurements in (9) can be expressed as*

$$\mathrm{Cov}\big(\hat{\boldsymbol{r}}_{\rm rx}(\boldsymbol{y})\big) \succeq \big(\mathbf{A}-\mathbf{B}\mathbf{D}^{-1}\mathbf{B}^T\big)^{-1} \tag{37}$$

where $\hat{\boldsymbol{r}}_{\rm rx}(\boldsymbol{y})$ is any unbiased estimate of $\boldsymbol{r}_{\rm rx}$, $\mathbf{A}$ is a 3×3 matrix specified as

$$[\mathbf{A}]_{l,m} = \sum_{k=1}^{N_{\rm M}} \frac{\sigma_k^2 a_{k,l}a_{k,m} + \tilde{\sigma}_k^2 b_{k,l}b_{k,m} + \gamma_k(a_{k,l}b_{k,m}+a_{k,m}b_{k,l})}{(\sigma_k^2\tilde{\sigma}_k^2-\gamma_k^2)^2} \tag{38}$$

for $l,m\in\{1,2,3\}$,

$$\mathbf{B} = -c\sum_{k=1}^{N_{\rm M}}\frac{1}{\sigma_k^2\tilde{\sigma}_k^2-\gamma_k^2}\begin{bmatrix} a_{k,1} & a_{k,1}kT+b_{k,1}\\ a_{k,2} & a_{k,2}kT+b_{k,2}\\ a_{k,3} & a_{k,3}kT+b_{k,3}\end{bmatrix}, \tag{39}$$

and

$$\mathbf{D} = c^2\sum_{k=1}^{N_{\rm M}}\frac{1}{\sigma_k^2\tilde{\sigma}_k^2-\gamma_k^2}\times \begin{bmatrix} \tilde{\sigma}_k^2 & \tilde{\sigma}_k^2(kT)-\gamma_k\\ \tilde{\sigma}_k^2(kT)-\gamma_k & \tilde{\sigma}_k^2(kT)^2-2\gamma_k(kT)+\sigma_k^2\end{bmatrix}. \tag{40}$$

The $a_{k,l}$ and $b_{k,l}$ terms in (38) and (39) are defined as

$$a_{k,l} \triangleq \tilde{\sigma}_k^2\frac{\partial f_k(\boldsymbol{r}_{\rm rx})}{\partial r_{\rm rx}^l} - \gamma_k\frac{\partial g_k(\boldsymbol{r}_{\rm rx})}{\partial r_{\rm rx}^l}, \tag{41}$$

$$b_{k,l} \triangleq \sigma_k^2\frac{\partial g_k(\boldsymbol{r}_{\rm rx})}{\partial r_{\rm rx}^l} - \gamma_k\frac{\partial f_k(\boldsymbol{r}_{\rm rx})}{\partial r_{\rm rx}^l}, \tag{42}$$

with

$$\frac{\partial f_k(\boldsymbol{r}_{\rm rx})}{\partial r_{\rm rx}^l} = -\frac{\big(r_{\rm rx}^l - r_{\rm leo}^l(k')\big)}{\|\boldsymbol{r}_{\rm rx}-\boldsymbol{r}_{\rm leo}(k')\|}, \tag{43}$$

$$\frac{\partial g_k(\boldsymbol{r}_{\rm rx})}{\partial r_{\rm rx}^l} = \frac{\dot{r}_{\rm leo}^l(k')}{\|\boldsymbol{r}_{\rm rx}-\boldsymbol{r}_{\rm leo}(k')\|} - \frac{\dot{\boldsymbol{r}}_{\rm leo}(k')^T(\boldsymbol{r}_{\rm rx}-\boldsymbol{r}_{\rm leo}(k'))\big(r_{\rm rx}^l-r_{\rm leo}^l(k')\big)}{\|\boldsymbol{r}_{\rm rx}-\boldsymbol{r}_{\rm leo}(k')\|^3} \tag{44}$$

for $l=1,2,3$ and $k=1,\ldots,N_{\rm M}$, where $r_{\rm rx}^l$, $r_{\rm leo}^l(k')$, and $\dot{r}_{\rm leo}^l(k')$ denote the lth components of $\boldsymbol{r}_{\rm rx}$, $\boldsymbol{r}_{\rm leo}(k')$, and $\dot{\boldsymbol{r}}_{\rm leo}(k')$, respectively.

Proof: Based on the definitions in (15), (16), (18), (19), (24), and (25), the log-likelihood function $\log p(\boldsymbol{y}|\boldsymbol{\theta})$ in (21), called $\mathcal{L}$ for simplicity, can be shown to be proportional to (cf. (34))

$$\mathcal{L}\propto -\frac{1}{2}\sum_{k=1}^{N_{\rm M}}\frac{1}{\sigma_k^2\tilde{\sigma}_k^2-\gamma_k^2}\Big(\tilde{\sigma}_k^2(f_k(\boldsymbol{r}_{\rm rx})-cb-kcTd)^2 - 2\gamma_k\times (f_k(\boldsymbol{r}_{\rm rx})-cb-kcTd)(g_k(\boldsymbol{r}_{\rm rx})-cd) + \sigma_k^2(g_k(\boldsymbol{r}_{\rm rx})-cd)^2\Big) \tag{45}$$

Then, the partial derivatives of (45) with respect to the elements of $\boldsymbol{\theta}=[\boldsymbol{r}_{\rm rx},b,d]^T$ can be calculated as follows:

$$\frac{\partial\mathcal{L}}{\partial r_{\rm rx}^l} = -\sum_{k=1}^{N_{\rm M}}\frac{1}{\sigma_k^2\tilde{\sigma}_k^2-\gamma_k^2}\big(a_{k,l}(f_k(\boldsymbol{r}_{\rm rx})-cb-kcTd) + b_{k,l}(g_k(\boldsymbol{r}_{\rm rx})-cd)\big) \tag{46}$$

for $l=1,2,3$, where $r_{\rm rx}^l$ denotes the lth element of $\boldsymbol{r}_{\rm rx}$, and $a_{k,l}$ and $b_{k,l}$ are as defined in (41) and (42),

$$\frac{\partial\mathcal{L}}{\partial b} = c\sum_{k=1}^{N_{\rm M}}\frac{1}{\sigma_k^2\tilde{\sigma}_k^2-\gamma_k^2}\big(\tilde{\sigma}_k^2(f_k(\boldsymbol{r}_{\rm rx})-cb-kcTd) - \gamma_k(g_k(\boldsymbol{r}_{\rm rx})-cd)\big), \tag{47}$$

$$\frac{\partial\mathcal{L}}{\partial d} = c\sum_{k=1}^{N_{\rm M}}\frac{1}{\sigma_k^2\tilde{\sigma}_k^2-\gamma_k^2}\big((\tilde{\sigma}_k^2kT-\gamma_k)(f_k(\boldsymbol{r}_{\rm rx})-cb-kcTd) + (\sigma_k^2-\gamma_k kT)(g_k(\boldsymbol{r}_{\rm rx})-cd)\big). \tag{48}$$

Then, the 5×5 FIM can be formed as

$$\mathbf{J}(\boldsymbol{\theta}) = \begin{bmatrix}\mathbf{A} & \mathbf{B}\\ \mathbf{B}^T & \mathbf{D}\end{bmatrix} \tag{49}$$

where

$$[\mathbf{A}]_{l,m} = \mathbb{E}\left\{\frac{\partial\mathcal{L}}{\partial r_{\rm rx}^l}\frac{\partial\mathcal{L}}{\partial r_{\rm rx}^m}\right\} \tag{50}$$

for $l,m\in\{1,2,3\}$,

$$[\mathbf{B}]_{l,1} = \mathbb{E}\left\{\frac{\partial\mathcal{L}}{\partial r_{\rm rx}^l}\frac{\partial\mathcal{L}}{\partial b}\right\},\quad [\mathbf{B}]_{l,2} = \mathbb{E}\left\{\frac{\partial\mathcal{L}}{\partial r_{\rm rx}^l}\frac{\partial\mathcal{L}}{\partial d}\right\} \tag{51}$$

for $l\in\{1,2,3\}$,

$$[\mathbf{D}]_{1,1} = \mathbb{E}\left\{\left(\frac{\partial\mathcal{L}}{\partial b}\right)^2\right\},\quad [\mathbf{D}]_{2,2} = \mathbb{E}\left\{\left(\frac{\partial\mathcal{L}}{\partial d}\right)^2\right\},$$
$$[\mathbf{D}]_{1,2} = [\mathbf{D}]_{2,1} = \mathbb{E}\left\{\frac{\partial\mathcal{L}}{\partial b}\frac{\partial\mathcal{L}}{\partial d}\right\}. \tag{52}$$

From the expressions in (46)–(48), the elements of the FIM in (49), namely, the elements of $\mathbf{A}$, $\mathbf{B}$, and $\mathbf{D}$ in (50)–(52) can be calculated, after some manipulation, as in (38)–(40) in Lemma 2. Then, the CRLB for the receiver position can be obtained from the block matrix inversion formula as follows:

$$\mathrm{Cov}\big(\hat{\boldsymbol{r}}_{\rm rx}(\boldsymbol{y})\big) \succeq \big[\mathbf{J}(\boldsymbol{\theta})^{-1}\big]_{3\times 3} = \big(\mathbf{A}-\mathbf{B}\mathbf{D}^{-1}\mathbf{B}^T\big)^{-1} \tag{53}$$

which corresponds to the expression in (37) of Lemma 2. Also, the partial derivatives of the $f_k(\boldsymbol{r}_{\rm rx})$ and $g_k(\boldsymbol{r}_{\rm rx})$ terms presented in (43) and (44) can directly be obtained from (24) and (25). ■

The CRLB expression in Lemma 2 can be evaluated for any generic scenario to calculate the lower bound on the MSE of unbiased position estimators in localization systems utilizing pseudorange and pseudorange rate (Doppler) measurements from a single LEO satellite. Since the matrices in the CRLB expression in (37) are presented in closed forms, the main complexity of the CRLB calculation is related to the 3×3 matrix inversion in (37). Hence, it can be calculated rapidly for any given setting.

Remark 3: For the existence of the CRLB in (37), it is required that $\sigma_k^2 \tilde{\sigma}_k^2 - \gamma_k^2 > 0$ for all $k \in \{1, \ldots, N_{\rm M}\}$ and $\mathbf{D}$ is positive definite. These conditions hold since the noise covariance sub-matrices, $\mathbf{R}_k$'s in (12), are assumed to be positive definite. In addition, $(\mathbf{A} - \mathbf{B}\mathbf{D}^{-1}\mathbf{B}^T)$ becomes positive definite when the line-of-sight (LOS) directions between the receiver and the satellite and the transverse components of the relative velocity vary across the time epochs so that the induced pseudorange and pseudorange rate gradients collectively span $\mathbb{R}^3$. □

For comparison purposes, the CRLBs for position estimation are also calculated in the presence of only pseudorange measurements or only pseudorange rate measurements in the following. (The proofs are not presented due to the space limitation, which can be regarded as the special cases of Lemma 2.)

Corollary 1: *Let $\boldsymbol{y}_\rho \triangleq [\rho(1), \ldots, \rho(N_{\rm M})]^T$ represent the vector of pseudorange measurements in (6). The CRLB on the estimation of the receiver position from the pseudorange measurements is given by*

$$\mathrm{Cov}\big(\hat{\boldsymbol{r}}_{\rm rx}(\boldsymbol{y}_\rho)\big) \succeq \left(\mathbf{A}_\rho - \mathbf{B}_\rho \mathbf{D}_\rho^{-1} \mathbf{B}_\rho^T\right)^{-1} \tag{54}$$

where $\hat{\boldsymbol{r}}_{\rm rx}(\boldsymbol{y}_\rho)$ is any unbiased estimate of $\boldsymbol{r}_{\rm rx}$ based on $\boldsymbol{y}_\rho$,

$$[\mathbf{A}_\rho]_{l,m} = \sum_{k=1}^{N_{\rm M}} \frac{1}{\sigma_k^2} \frac{\partial f_k(\boldsymbol{r}_{\rm rx})}{\partial r_{\rm rx}^l} \frac{\partial f_k(\boldsymbol{r}_{\rm rx})}{\partial r_{\rm rx}^m} \tag{55}$$

for $l, m \in \{1, 2, 3\}$,

$$\mathbf{B}_\rho = -c \sum_{k=1}^{N_{\rm M}} \frac{1}{\sigma_k^2} \begin{bmatrix} \frac{\partial f_k(\boldsymbol{r}_{\rm rx})}{\partial r_{\rm rx}^1} & kT \frac{\partial f_k(\boldsymbol{r}_{\rm rx})}{\partial r_{\rm rx}^1} \\ \frac{\partial f_k(\boldsymbol{r}_{\rm rx})}{\partial r_{\rm rx}^2} & kT \frac{\partial f_k(\boldsymbol{r}_{\rm rx})}{\partial r_{\rm rx}^2} \\ \frac{\partial f_k(\boldsymbol{r}_{\rm rx})}{\partial r_{\rm rx}^3} & kT \frac{\partial f_k(\boldsymbol{r}_{\rm rx})}{\partial r_{\rm rx}^3} \end{bmatrix}, \tag{56}$$

and

$$\mathbf{D}_\rho = c^2 \sum_{k=1}^{N_{\rm M}} \frac{1}{\sigma_k^2} \begin{bmatrix} 1 & kT \\ kT & (kT)^2 \end{bmatrix}, \tag{57}$$

with $\partial f_k(\boldsymbol{r}_{\rm rx})/\partial r_{\rm rx}^l$ being given by (43).

In this case, the invertibility of $\mathbf{D}_\rho$ in (57) is guaranteed for $N_{\rm M} \geq 2$. In addition, for the existence of the CRLB in (54), there should be sufficient variations of the pseudorange measurements over the observation time [9].

Corollary 2: *Let $\boldsymbol{y}_{\dot\rho} \triangleq [\dot\rho(1), \ldots, \dot\rho(N_{\rm M})]^T$ represent the vector of pseudorange rate measurements in (7). The CRLB on the estimation of the receiver position from the pseudorange rate measurements is given by*

$$\mathrm{Cov}\big(\hat{\boldsymbol{r}}_{\rm rx}(\boldsymbol{y}_{\dot\rho})\big) \succeq \left(\mathbf{A}_{\dot\rho} - \mathbf{B}_{\dot\rho} \mathbf{B}_{\dot\rho}^T / D_{\dot\rho}\right)^{-1} \tag{58}$$

where $\hat{\boldsymbol{r}}_{\rm rx}(\boldsymbol{y}_{\dot\rho})$ is any unbiased estimate of $\boldsymbol{r}_{\rm rx}$ based on $\boldsymbol{y}_{\dot\rho}$,

$$[\mathbf{A}_{\dot\rho}]_{l,m} = \sum_{k=1}^{N_{\rm M}} \frac{1}{\tilde\sigma_k^2} \frac{\partial g_k(\boldsymbol{r}_{\rm rx})}{\partial r_{\rm rx}^l} \frac{\partial g_k(\boldsymbol{r}_{\rm rx})}{\partial r_{\rm rx}^m} \tag{59}$$

for $l, m \in \{1, 2, 3\}$,

$$\mathbf{B}_{\dot\rho} = -c \sum_{k=1}^{N_{\rm M}} \frac{1}{\tilde\sigma_k^2} \begin{bmatrix} \frac{\partial g_k(\boldsymbol{r}_{\rm rx})}{\partial r_{\rm rx}^1} \\ \frac{\partial g_k(\boldsymbol{r}_{\rm rx})}{\partial r_{\rm rx}^2} \\ \frac{\partial g_k(\boldsymbol{r}_{\rm rx})}{\partial r_{\rm rx}^3} \end{bmatrix}, \tag{60}$$

and

$$D_{\dot\rho} = c^2 \sum_{k=1}^{N_{\rm M}} \frac{1}{\tilde\sigma_k^2}, \tag{61}$$

with $\partial g_k(\boldsymbol{r}_{\rm rx})/\partial r_{\rm rx}^l$ being given by (44).

In the presence of only pseudorange rate measurements, the unknown parameter b disappears (see (7)). Since the Doppler gradient lies in the plane orthogonal to the LOS direction, the CRLB in (58) does not exist for purely radial motions of the satellite or when the LOS distance is essentially constant over the observation interval.

IV. Simulation Results

A. Simulation Setup

In this section, we perform simulations to evaluate the performance of the MLE for the receiver position and compare it against the CRLB for various system parameters. We consider the setup in [9], consisting of a single LEO satellite and a ground receiver. The receiver is evaluated under different receiver-orbital plane geometries.

All vectors are expressed in the Earth-centered inertial (ECI) frame. Let R_E denote Earth's mean radius. The LEO satellite follows a circular orbit of altitude H and radius R_s with a fixed inclination, where $R_s = R_E + H$, and the mean motion parameter is given by $\varepsilon \triangleq \sqrt{\tilde\mu / R_s^3}$, with $\tilde\mu$ denoting Earth's gravitational parameter.[4] In the simulations, $R_E = 6378.137\,\mathrm{km}$, $\tilde\mu = 3.986 \times 10^5\,\mathrm{km}^3/\mathrm{s}^2$, and $H = 550\,\mathrm{km}$. Let $\boldsymbol{n}_{\rm orb} \in \mathbb{R}^3$ be a unit vector that is normal to the orbital plane, and let $\boldsymbol{p}, \boldsymbol{q} \in \mathbb{R}^3$ specify an orthonormal basis spanning the orbital plane, as shown in Fig. 1. Then, the satellite position and velocity can be modeled as

$$\boldsymbol{r}_{\rm leo}(t) = R_s \left(\cos\big(\varepsilon(t - t_0)\big)\, \boldsymbol{p} + \sin\big(\varepsilon(t - t_0)\big)\, \boldsymbol{q}\right), \tag{62}$$

$$\dot{\boldsymbol{r}}_{\rm leo}(t) = R_s \varepsilon \left(-\sin\big(\varepsilon(t - t_0)\big)\, \boldsymbol{p} + \cos\big(\varepsilon(t - t_0)\big)\, \boldsymbol{q}\right), \tag{63}$$

where t_0 is the reference time. Considering an inclination of $53°$, we set $\boldsymbol{n}_{\rm orb} = [0, -\sin(53°), \cos(53°)]^T / \|[0, -\sin(53°), \cos(53°)]\|$,

[4]Although a simplified circular-orbit model is adopted in the simulations, the theoretical MLE and CRLB derivations are not specific to this particular orbital model or simulation geometry. They can directly be evaluated using more realistic satellite trajectories and geometry [45].

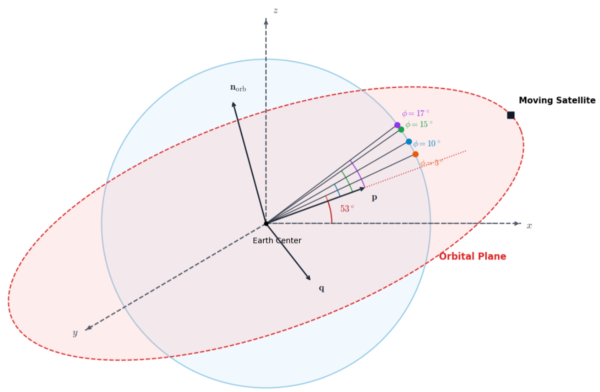

Fig. 1. System setup in the simulations.

$\boldsymbol{p} = [1, 0, 0]^T$, and $\boldsymbol{q} = \boldsymbol{n}_{\mathrm{orb}} \times \boldsymbol{p}/\|\boldsymbol{n}_{\mathrm{orb}} \times \boldsymbol{p}\|$, where $\times$ denotes the cross product.

The receiver is fixed on Earth's surface and is modeled as stationary in the ECI frame over the observation interval. Let $\hat{\boldsymbol{r}}_{\mathrm{rx}}$ denote the unit ECI direction of the receiver from Earth's center. The receiver position is defined as

$$\boldsymbol{r}_{\mathrm{rx}} = R_E\,\hat{\boldsymbol{r}}_{\mathrm{rx}} \in \mathbb{R}^3, \tag{64}$$

where $\boldsymbol{r}_{\mathrm{rx}}$ denotes the receiver position. To define the receiver position with respect to the orbital plane as in [9], we express $\hat{\boldsymbol{r}}_{\mathrm{rx}}$ in terms of the receiver-orbital plane angle (ϕ) as

$$\hat{\boldsymbol{r}}_{\mathrm{rx}} = \cos\phi\,\boldsymbol{p} + \sin\phi\,\boldsymbol{n}_{\mathrm{orb}}, \tag{65}$$

such that $\left|\hat{\boldsymbol{r}}_{\mathrm{rx}}^T \boldsymbol{n}_{\mathrm{orb}}\right| = \sin\phi$. As shown in Fig. 1, the receiver-orbital plane angle is set to $\phi = 5°$, $10°$, $15°$ and $17°$ to evaluate four different receiver-orbit geometries.

In the simulations, we collect N_{M} measurements at times $t_k = t_0 + kT$ for $k = 1, \ldots, N_{\mathrm{M}}$, with a sampling period of $T = 10$ seconds (unless stated otherwise). The standard deviations of the measurement noises in (12) are assumed to be identical across the measurements; i.e., $\sigma_1 = \cdots = \sigma_{N_{\mathrm{M}}} \triangleq \sigma$ and $\tilde{\sigma}_1 = \cdots = \tilde{\sigma}_{N_{\mathrm{M}}} \triangleq \tilde{\sigma}$. Similarly, the correlation parameters in (12) are taken to be constant such that $\gamma_1 = \cdots = \gamma_{N_{\mathrm{M}}} \triangleq \gamma$.

Let $\hat{\boldsymbol{u}}_{k,i}$ denote the LOS unit vector from receiver i to the satellite (evaluated at time t'_k). A *pass* for receiver i is the contiguous set of time epochs for which the satellite satisfies the visibility constraints. Specifically, to ensure a realistic observation model [12], we define a maximum zenith angle threshold as $\zeta_{\max} = 85°$. A measurement is valid if the zenith angle $\zeta_{k,i}^{\mathrm{zen}} = \arccos\big(\hat{\boldsymbol{u}}_{k,i}^T \hat{\boldsymbol{r}}_{\mathrm{rx}}^{(i)}\big)$ satisfies $\zeta_{k,i}^{\mathrm{zen}} \leq \zeta_{\max}$, which corresponds to a minimum elevation angle of $\mathrm{el}_{\min} = 90° - \zeta_{\max} = 5°$ [12]. Each receiver collects measurements as in (6) and (7). Since the clock parameters of the satellite are assumed to be known, the $\delta t_{\mathrm{leo}}(k')$ and $\dot{\delta t}_{\mathrm{leo}}(k')$ terms are set to zero in (6) and (7) without loss of generality (i.e., it is assumed that the measurements are pre-corrected based on the known clock parameters of the satellite).

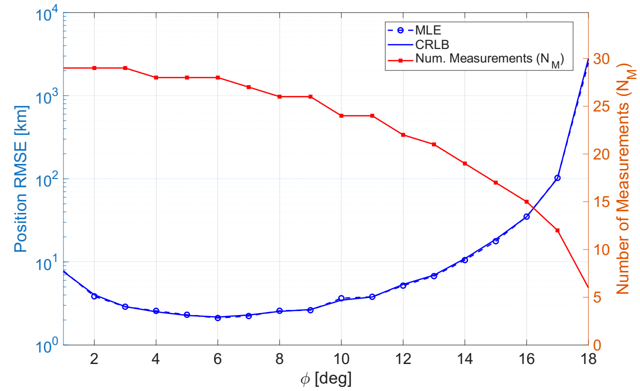

Fig. 2. RMSE of the MLE, the CRLB, and the number of available measurements as a function of receiver-orbital plane angle, where $\sigma = 1.3 \times 10^{-3}$ km, $\tilde{\sigma} = 0.7 \times 10^{-3}$ km/s, and $\gamma = 0$.

B. Performance Evaluation

For the implementation of the proposed MLE in Lemma 1, we employ the following two-step optimization strategy: (i) First, a coarse grid search is performed over a three-dimensional Cartesian box centered around a randomly perturbed initial receiver position. For each grid point, the clock bias and clock drift are computed in closed form as in Lemma 1, and the corresponding objective function in (23) is evaluated.[5] The grid point with the lowest objective value is selected as the initial point for iterative optimization in the next step. (ii) Starting from this initial point, the nonlinear problem in (23) is solved using the Levenberg–Marquardt algorithm implemented by the `lsqnonlin` function in MATLAB.

Before focusing on the three receiver positions shown in Fig. 1, we first investigate the effects of the receiver-orbital plane angle on the localization performance. To this aim, Fig. 2 illustrates the maximum number of available measurements corresponding to various receiver-orbital plane angles by evaluating satellite visibility under the elevation constraint; namely, for a maximum zenith angle of 85° (or, a minimum elevation angle of 5°). In addition to the number of available measurements, the root mean-squared error (RMSE) of the MLE and the CRLB are also plotted on the same figure by using the left axis. For these simulations, the measurement noise parameters are set to $\sigma = 1.3 \times 10^{-3}$ km and $\tilde{\sigma} = 0.7 \times 10^{-3}$ km/s, which represent baseline values consistent with the average levels reported in [17], and the correlation

[5]In the simulations, the initial coarse-search grid is centered at a perturbed version of the true receiver position. Specifically, independent random offsets uniformly distributed over $[-50, 50]$ km are added to the three Cartesian coordinates of the true receiver position. Around this perturbed center, the grid points are generated with offsets $-100 : 25 : 100$ km along each Cartesian coordinate. Hence, the coarse grid contains 9 points per coordinate direction, resulting in $9^3 = 729$ candidate receiver positions.

parameter is taken to be zero; i.e., $\gamma = 0$. It is observed from Fig. 2 that the availability of measurements varies with receiver-orbital plane angle due to orbital geometry, directly influencing the achievable estimation accuracy. However, more measurements do not always result in lower estimation errors since the relative positions of the LEO satellite and the receiver affect the estimation performance, as well.

Fig. 3 presents the RMSEs of the MLEs and the CRLBs for the four distinct receiver-orbital plane angles with $\phi = 5°$, $10°$, $15°$, and $17°$ as shown in Fig. 1. In Fig. 3a, positioning performance is evaluated versus the standard deviation of the pseudorange measurement noise, σ, when $\tilde{\sigma} = 0.7 \times 10^{-3}\,\mathrm{km/s}$. On the other hand, in Fig. 3b, the performance evaluation is with respect to the standard deviation of the pseudorange rate noise $\tilde{\sigma}$ when $\sigma = 10^{-3}\,\mathrm{km}$. In both cases, the correlation between the pseudorange and pseudorange rate measurement noises is set to zero; that is, $\gamma = 0$. The results reveal that the lowest positioning errors are achieved at the $\phi = 5°$ among the four possible positions. As the receiver-orbital plane angle increases to $10°$, $15°$ and $17°$, a corresponding increase in the RMSE is observed due to the changes in satellite visibility, the number of available measurements, and geometry. Also, it is observed that the MLE consistently achieves a close performance to the CRLB in all the scenarios. Moreover, as the σ increases beyond a certain value, the pseudorange measurements become useless compared to the pseudorange rate (Doppler) measurements; hence, a constant RMSE is achieved on the right side of Fig. 3a. A similar observation is also made in Fig. 3b as $\tilde{\sigma}$ increases. Finally, it is noted that, for low noise deviations, the position can be estimated with dekameter level accuracy; however, for high values of σ or $\tilde{\sigma}$, the position error increases significantly, reaching levels above 100 km in Fig. 3a and above 10 km in Fig. 3b.

In Fig. 4, we investigate the effect of the number of measurements on the positioning performance by increasing the sampling period (T) from 10 seconds to 20 seconds while maintaining the same orbital geometry. The receiver-orbital plane angle is fixed at $\phi = 10°$ throughout this analysis. This effectively halves the number of measurements (N_{M}) for a given pass duration (namely, $N_{\mathrm{M}} = 24$ for $T = 10$ seconds while $N_{\mathrm{M}} = 12$ for $T = 20$ seconds). Fig. 4 depicts how this reduction in the number of measurements affects the positioning error by presenting the RMSEs of the MLEs and the CRLBs for various values of the noise standard deviations, where the correlation parameter, γ, is zero. Specifically, Fig. 4a illustrates the effect of varying the pseudorange measurement noise (σ) when $\tilde{\sigma} = 0.7{\times}10^{-3}\,\mathrm{km/s}$ whereas Fig. 4b shows the effect of varying the pseudorange rate noise ($\tilde{\sigma}$) when $\sigma = 1.3{\times}10^{-3}\,\mathrm{km}$. As expected, increasing the number of measurements from $N_{\mathrm{M}} = 12$ to $N_{\mathrm{M}} = 24$ results in a consistent reduction in the positioning error across all the considered noise levels.

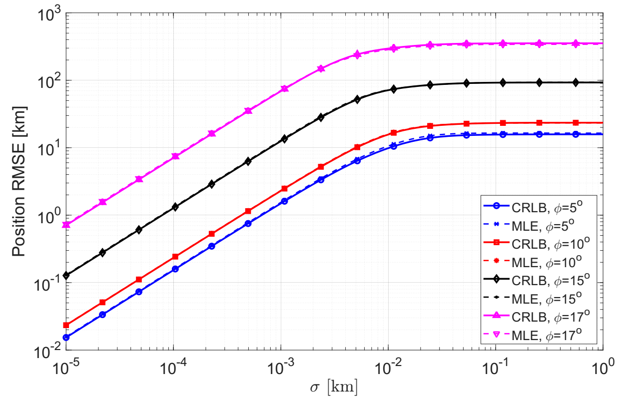

(a) RMSE of the MLE and the CRLB versus the standard deviation of the pseudorange measurement noise (σ) when $\tilde{\sigma} = 0.7 \times 10^{-3}\,\mathrm{km/s}$, $\bar{\gamma} = 0$.

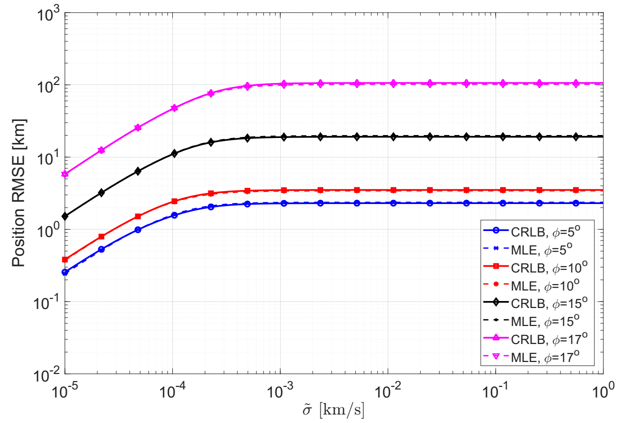

(b) RMSE of the MLE and the CRLB versus the standard deviation of the pseudorange rate measurement noise ($\tilde{\sigma}$) when $\sigma = 1.3{\times}10^{-3}\,\mathrm{km}$, $\bar{\gamma} = 0$.

Fig. 3. Comparison of the MLE and the CRLB for receiver locations at receiver-orbital plane angles $5°$, $10°$, $15°$, and $17°$.

Next, we investigate the positioning performance when the standard deviations of the pseudorange and pseudorange rate noise components change simultaneously. For this purpose, we employ a noise scaling factor k and set $\sigma = k{\times}1.3 \times 10^{-3}\,\mathrm{km}$ and $\tilde{\sigma} = k \times 0.7 \times 10^{-3}\,\mathrm{km/s}$. In Fig. 5, we plot the RMSE of the MLE and the CRLB versus k, where $T = 10$ seconds, $\gamma = 0$, and $\phi = 10°$. The results reveal that although the CRLB increases linearly with the noise scaling factor k in the logarithmic scale, the MLE performance deviates from this trend at higher noise levels ($k > 200$) and shows saturation characteristics. This saturation occurs since the search space for the MLE is geometrically bounded, preventing the estimation error from growing indefinitely. However, the CRLB does not utilize any prior information about the receiver position.

In certain practical scenarios, the noise components in the pseudorange and pseudorange rate measurements exhibit correlation. This correlation is implemented into the model via the covariance term γ, as mentioned before. In this part, we express γ as $\gamma = \bar{\gamma}\sigma\tilde{\sigma}$, where $\bar{\gamma}$ represents the correlation coefficient, and investigate

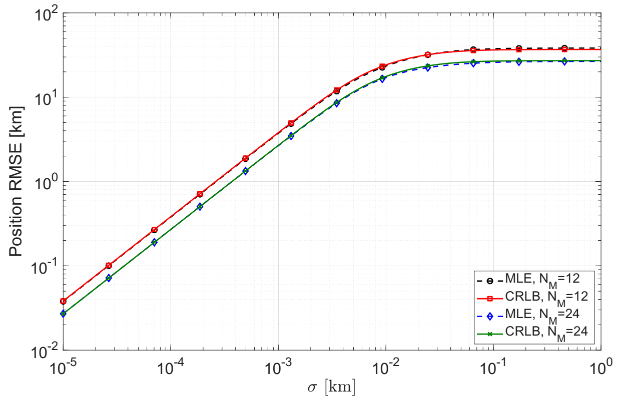

(a) RMSE of the MLE and the CRLB versus the standard deviation of the pseudorange measurement noise (σ) when $\tilde{\sigma} = 0.7 \times 10^{-3}$ km/s and $\gamma = 0$.

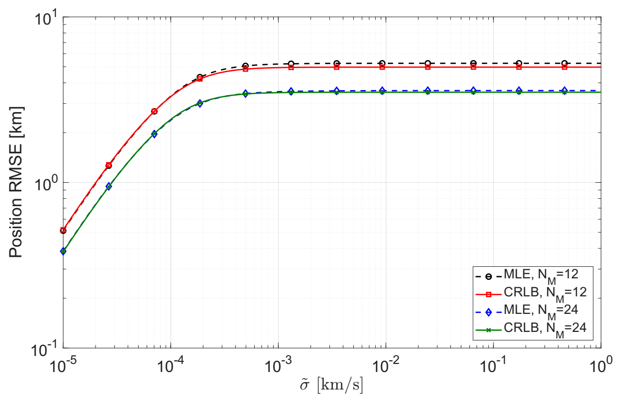

(b) RMSE of the MLE and the CRLB versus the standard deviation of the pseudorange rate measurement noise ($\tilde{\sigma}$) when $\sigma = 1.3 \times 10^{-3}$ km and $\gamma = 0$.

Fig. 4. Positioning performance versus the standard deviations of the pseudorange measurement noise and the pseudorange rate measurement noise for different numbers of measurements (N_{M}).

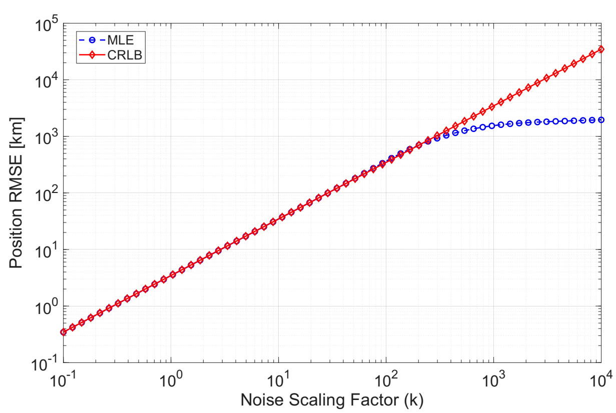

Fig. 5. RMSE of the MLE and the CRLB versus the noise scaling factor k when $\gamma = 0$.

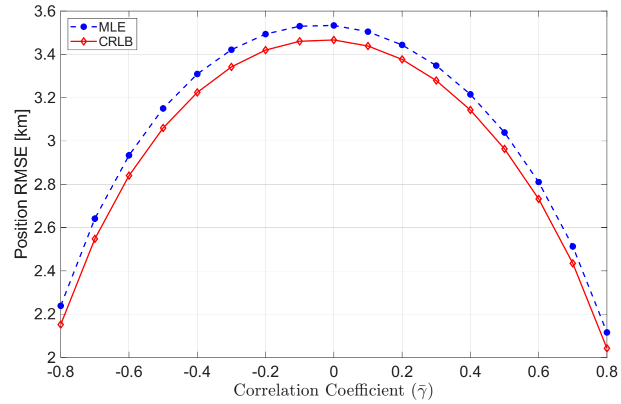

Fig. 6. Effects of measurement noise correlation coefficient, defined as $\bar{\gamma} = \gamma/(\sigma\,\tilde{\sigma})$, on the position estimation performance for $\sigma = 1.3 \times 10^{-3}$ km and $\tilde{\sigma} = 0.7 \times 10^{-3}$ km/s.

the positioning performance with respect to $\bar{\gamma}$ in Fig. 6 by setting $\sigma = 1.3 \times 10^{-3}$ km, $\tilde{\sigma} = 0.7 \times 10^{-3}$ km/s, $T = 10$ seconds, and a receiver-orbital plane angle of $\phi = 10°$. The results indicate that increasing the absolute value of the correlation coefficient leads to a reduction in both the position RMSE obtained by the MLE and the corresponding CRLB. This phenomenon, increased correlation leading to improved accuracy, is caused by the structure of the noise model where stronger correlation between pseudorange and pseudorange rate measurement noises reduces overall uncertainty of the combined measurements. In other words, noise mitigation becomes more effective when the noise components in given time epochs are more correlated.

Finally, Fig. 7 provides a direct comparison between two distinct correlation scenarios: $\bar{\gamma} = 0$ (uncorrelated) and $\bar{\gamma} = 0.5$ for a sampling period of $T = 10$ seconds and with receiver-orbital plane angle of $10°$. While in Fig. 7a, the positioning performance is simulated versus the standard deviation of the pseudorange measurement noise, σ, when $\tilde{\sigma} = 0.7 \times 10^{-3}$ km/s, Fig. 7b shows the performance evaluation with respect to the standard deviation of the pseudorange rate noise $\tilde{\sigma}$ when $\sigma = 1.3 \times 10^{-3}$ km. It is observed that the presence of measurement correlation ($\bar{\gamma} = 0.5$) leads to improved positioning performance compared to the uncorrelated scenario ($\bar{\gamma} = 0$). As illustrated in both figures, the RMSE curves corresponding to $\bar{\gamma} = 0.5$ consistently remain below those of the uncorrelated cases, indicating that the MLE benefits from the correlation information about the noise components to mitigate the effects of noise on the position estimation accuracy.

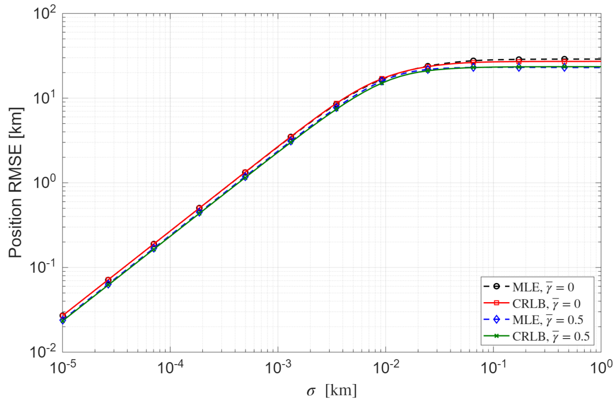

(a) Positioning error versus the standard deviation of the pseudorange measurement noise (σ) when $\tilde{\sigma} = 0.7 \times 10^{-3}\,\mathrm{km/s}$ for different correlation coefficients ($\bar{\gamma}$).

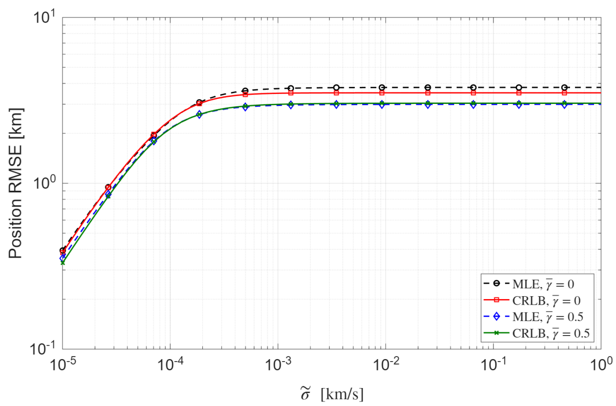

(b) Positioning error versus the standard deviation of the pseudorange rate measurement noise ($\tilde{\sigma}$) when $\sigma = 1.3 \times 10^{-3}\,\mathrm{km}$ for different correlation coefficients ($\bar{\gamma}$).

Fig. 7. Impact of measurement noise correlation on position estimation performance.

C. Comparison with Benchmarks

In this subsection, we compare the proposed MLE approach specified in Lemma 1 with several benchmark estimators in order to illustrate the effectiveness of the proposed estimation framework, which explicitly accounts for correlations between the measurement noise components. The considered benchmarks are the pseudorange-only MLE, the Doppler-only MLE, and the joint MLE that ignores the correlation between the noise components in the pseudorange and Doppler measurements in each time epoch (called "correlation-ignorant MLE"). The pseudorange-only and Doppler-only estimators are obtained by minimizing the corresponding likelihood functions constructed from only the pseudorange and pseudorange-rate (Doppler) measurements, respectively. Hence, they serve as benchmark cases for evaluating the performance gains achieved by the proposed MLE. In addition, the performance of the correlation-ignorant MLE provides an illustration for the effects of correlation in the measurement noise components.

The preceding benchmark estimators can be derived as special cases of the proposed MLE in Lemma 1, and are presented as follows:

- Doppler-only (Pseudorange rate-only) MLE: In this case, only the pseudorange rate measurements are used, and the corresponding MLE can be obtained by considering it as a special case of Lemma 1 as

$$\hat{\boldsymbol{r}}^{\mathrm{do}}_{\mathrm{rx}}(\boldsymbol{y}) = \underset{\boldsymbol{r}_{\mathrm{rx}} \in \mathcal{S}_{\mathrm{rx}}}{\arg\min} \sum_{k=1}^{N_{\mathrm{M}}} \frac{\left(g_k(\boldsymbol{r}_{\mathrm{rx}}) - c\,\hat{d}^{\mathrm{do}}(\boldsymbol{r}_{\mathrm{rx}})\right)^2}{\tilde{\sigma}_k^2}$$

where

$$\hat{d}^{\mathrm{do}}(\boldsymbol{r}_{\mathrm{rx}}) = \frac{\beta_0^{\mathrm{do}}(\boldsymbol{r}_{\mathrm{rx}})}{\beta_2^{\mathrm{do}}},$$

with

$$\beta_0^{\mathrm{do}}(\boldsymbol{r}_{\mathrm{rx}}) \triangleq \sum_{k=1}^{N_{\mathrm{M}}} \frac{g_k(\boldsymbol{r}_{\mathrm{rx}})}{\tilde{\sigma}_k^2},$$

$$\beta_2^{\mathrm{do}} \triangleq c \sum_{k=1}^{N_{\mathrm{M}}} \frac{1}{\tilde{\sigma}_k^2}.$$

In this case, since the receiver clock bias does not appear in the Doppler-only measurement model, only the clock drift parameter is estimated for each possible receiver position.

- Pseudorange-only MLE: In this case, only the pseudorange measurements are used, and the corresponding MLE is implemented as

$$\hat{\boldsymbol{r}}^{\mathrm{po}}_{\mathrm{rx}}(\boldsymbol{y}) = \underset{\boldsymbol{r}_{\mathrm{rx}} \in \mathcal{S}_{\mathrm{rx}}}{\arg\min} \sum_{k=1}^{N_{\mathrm{M}}} \frac{\left(f_k(\boldsymbol{r}_{\mathrm{rx}}) - c\,\hat{b}^{\mathrm{po}}(\boldsymbol{r}_{\mathrm{rx}}) - kcT\hat{d}^{\mathrm{po}}(\boldsymbol{r}_{\mathrm{rx}})\right)^2}{\sigma_k^2}.$$

Here, the clock bias and clock drift estimates for a fixed receiver position are given by (cf. Lemma 1)

$$\begin{bmatrix} \hat{b}^{\mathrm{po}}(\boldsymbol{r}_{\mathrm{rx}}) \\ \hat{d}^{\mathrm{po}}(\boldsymbol{r}_{\mathrm{rx}}) \end{bmatrix} = \frac{1}{\alpha_1^{\mathrm{po}}\beta_2^{\mathrm{po}} - (\alpha_2^{\mathrm{po}})^2} \times \begin{bmatrix} \alpha_0^{\mathrm{po}}(\boldsymbol{r}_{\mathrm{rx}})\beta_2^{\mathrm{po}} - \alpha_2^{\mathrm{po}}\beta_0^{\mathrm{po}}(\boldsymbol{r}_{\mathrm{rx}}) \\ \alpha_1^{\mathrm{po}}\beta_0^{\mathrm{po}}(\boldsymbol{r}_{\mathrm{rx}}) - \alpha_0^{\mathrm{po}}(\boldsymbol{r}_{\mathrm{rx}})\alpha_2^{\mathrm{po}} \end{bmatrix},$$

where

$$\alpha_0^{\mathrm{po}}(\boldsymbol{r}_{\mathrm{rx}}) \triangleq \sum_{k=1}^{N_{\mathrm{M}}} \frac{f_k(\boldsymbol{r}_{\mathrm{rx}})}{\sigma_k^2},$$

$$\alpha_1^{\mathrm{po}} \triangleq c \sum_{k=1}^{N_{\mathrm{M}}} \frac{1}{\sigma_k^2},$$

$$\alpha_2^{\mathrm{po}} \triangleq c \sum_{k=1}^{N_{\mathrm{M}}} \frac{kT}{\sigma_k^2},$$

$$\beta_0^{\mathrm{po}}(\boldsymbol{r}_{\mathrm{rx}}) \triangleq \sum_{k=1}^{N_{\mathrm{M}}} \frac{kTf_k(\boldsymbol{r}_{\mathrm{rx}})}{\sigma_k^2},$$

$$\beta_2^{\mathrm{po}} \triangleq c \sum_{k=1}^{N_{\mathrm{M}}} \frac{(kT)^2}{\sigma_k^2}.$$

- Correlation-ignorant MLE: In this case, both the pseudorange and pseudorange rate measurements are used, but it is assumed that the pseudorange and pseudorange rate measurements are independent in each epoch. The resulting estimator can be obtained as

$$\hat{\boldsymbol{r}}_{\mathrm{rx}}^{\mathrm{ci}}(\boldsymbol{y}) = \underset{\boldsymbol{r}_{\mathrm{rx}} \in \mathcal{S}_{\mathrm{rx}}}{\arg\min} \sum_{k=1}^{N_{\mathrm{M}}} \frac{\left(f_k(\boldsymbol{r}_{\mathrm{rx}}) - c\hat{b}^{\mathrm{ci}}(\boldsymbol{r}_{\mathrm{rx}}) - kcT\hat{d}^{\mathrm{ci}}(\boldsymbol{r}_{\mathrm{rx}})\right)^2}{\sigma_k^2} + \frac{\left(g_k(\boldsymbol{r}_{\mathrm{rx}}) - c\hat{d}^{\mathrm{ci}}(\boldsymbol{r}_{\mathrm{rx}})\right)^2}{\tilde{\sigma}_k^2}.$$

Here, the clock bias and clock drift estimates for a fixed receiver position are given by (cf. Lemma 1)

$$\begin{bmatrix} \hat{b}^{\mathrm{ci}}(\boldsymbol{r}_{\mathrm{rx}}) \\ \hat{d}^{\mathrm{ci}}(\boldsymbol{r}_{\mathrm{rx}}) \end{bmatrix} = \frac{1}{\alpha_1^{\mathrm{ci}}\beta_2^{\mathrm{ci}} - \left(\alpha_2^{\mathrm{ci}}\right)^2} \times \begin{bmatrix} \alpha_0^{\mathrm{ci}}(\boldsymbol{r}_{\mathrm{rx}})\beta_2^{\mathrm{ci}} - \alpha_2^{\mathrm{ci}}\beta_0^{\mathrm{ci}}(\boldsymbol{r}_{\mathrm{rx}}) \\ \alpha_1^{\mathrm{ci}}\beta_0^{\mathrm{ci}}(\boldsymbol{r}_{\mathrm{rx}}) - \alpha_0^{\mathrm{ci}}(\boldsymbol{r}_{\mathrm{rx}})\alpha_2^{\mathrm{ci}} \end{bmatrix},$$

where

$$\alpha_0^{\mathrm{ci}}(\boldsymbol{r}_{\mathrm{rx}}) \triangleq \sum_{k=1}^{N_{\mathrm{M}}} \frac{f_k(\boldsymbol{r}_{\mathrm{rx}})}{\sigma_k^2},$$

$$\alpha_1^{\mathrm{ci}} \triangleq c\sum_{k=1}^{N_{\mathrm{M}}} \frac{1}{\sigma_k^2},$$

$$\alpha_2^{\mathrm{ci}} \triangleq c\sum_{k=1}^{N_{\mathrm{M}}} \frac{kT}{\sigma_k^2},$$

$$\beta_0^{\mathrm{ci}}(\boldsymbol{r}_{\mathrm{rx}}) \triangleq \sum_{k=1}^{N_{\mathrm{M}}} \left(\frac{kTf_k(\boldsymbol{r}_{\mathrm{rx}})}{\sigma_k^2} + \frac{g_k(\boldsymbol{r}_{\mathrm{rx}})}{\tilde{\sigma}_k^2}\right),$$

$$\beta_2^{\mathrm{ci}} \triangleq c\sum_{k=1}^{N_{\mathrm{M}}} \left(\frac{(kT)^2}{\sigma_k^2} + \frac{1}{\tilde{\sigma}_k^2}\right).$$

For comparisons with these benchmark algorithms, we perform simulations when the receiver-orbital plane angle is chosen as $\phi = 10^\circ$ and the sampling time is $T = 10\,\mathrm{s}$. Fig. 8 presents the RMSEs of the proposed MLE and the pseudorange-only MLE for various standard deviations of the pseudorange measurement noise, σ, when $\tilde{\sigma} = 0.7 \times 10^{-3}\,\mathrm{km/s}$ and the correlation is $\bar{\gamma} = 0.5$. It is observed from the figure that both estimators provide almost identical performance at low and moderate pseudorange noise levels. This indicates that, in this region, the pseudorange measurements are sufficiently accurate and dominate the positioning performance. However, as σ increases, the pseudorange-only MLE exhibits a rapid degradation since its estimation accuracy depends solely on the quality of the pseudorange measurements. In contrast, the proposed MLE maintains a significantly lower RMSE at high pseudorange noise levels by exploiting the additional information provided by the Doppler measurements. Therefore, the proposed formulation is affected less severely by the increase in pseudorange noise and prevents the positioning error from increasing significantly as in the pseudorange-only case.

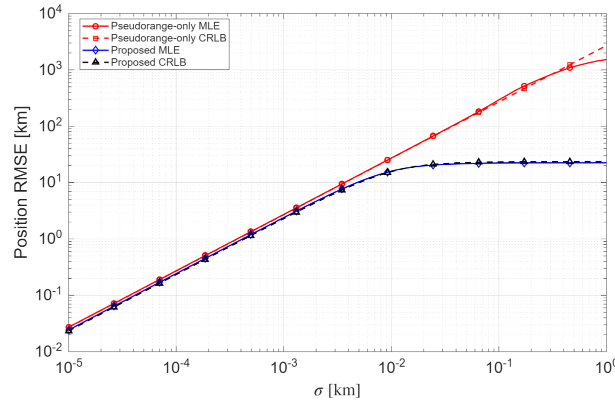

Fig. 8. RMSE of pseudorange-only MLE and proposed MLE versus the standard deviation of the pseudorange measurement noise (σ) when $\tilde{\sigma} = 0.7 \times 10^{-3}\,\mathrm{km/s}$ and $\bar{\gamma} = 0.5$.

In Fig. 9, the proposed MLE is compared with the Doppler-only MLE approach for various standard deviations, $\tilde{\sigma}$, of the pseudorange rate noise, when $\sigma = 1.3 \times 10^{-3}\,\mathrm{km}$ and the correlation parameter is $\bar{\gamma} = 0.5$. For small values of $\tilde{\sigma}$, both methods provide similar RMSE performance, since the Doppler measurements are sufficiently accurate and dominate the estimation accuracy in this region. However, as $\tilde{\sigma}$ increases, the RMSE of the Doppler-only MLE increases significantly since it relies only on pseudorange-rate measurements. In contrast, the RMSE of the proposed MLE remains saturated for large values of $\tilde{\sigma}$ by also benefiting from pseudorange measurements. Therefore, when the Doppler measurements become noisy, the proposed method can still benefit from the range information provided by the pseudorange measurements and achieves a lower positioning error than the Doppler-only estimator.

Next, we compare the proposed MLE versus the correlation-ignorant MLE, which assumes that the measurement noise components are uncorrelated. Fig. 10 shows a comparison of the proposed MLE against the

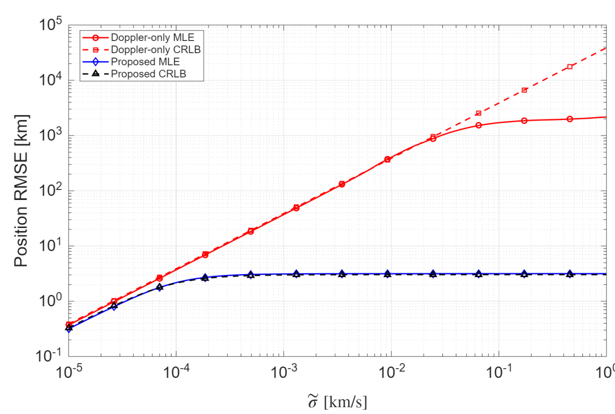

Fig. 9. RMSE of Doppler-only MLE and proposed MLE versus the standard deviation of the pseudorange-rate measurement noise ($\tilde{\sigma}$) when $\sigma = 1.3 \times 10^{-3}\,\mathrm{km}$ and $\bar{\gamma} = 0.5$.

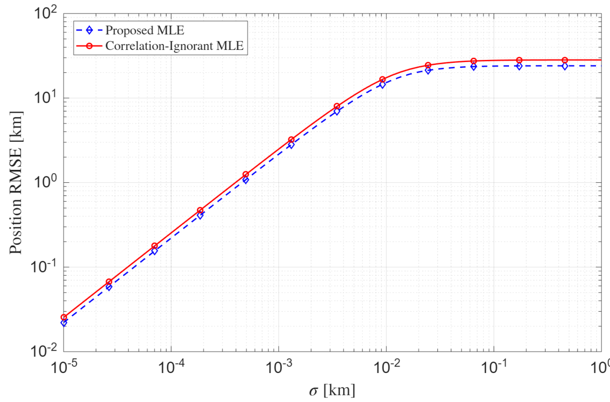

Fig. 10. RMSE of proposed MLE and correlation-ignorant MLE versus the standard deviation of the pseudorange measurement noise (σ) when $\tilde{\sigma} = 0.7 \times 10^{-3}$ km/s and $\bar{\gamma} = 0.5$.

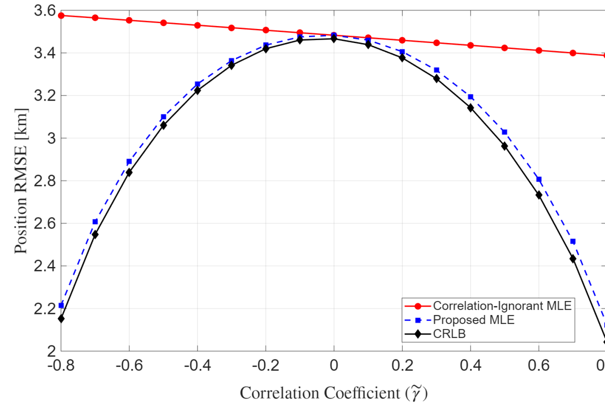

Fig. 12. Effects of measurement noise correlation coefficient, defined as $\bar{\gamma} = \gamma/(\sigma\,\tilde{\sigma})$, on the position estimation performance of proposed MLE and correlation-ignorant MLE for $\sigma = 1.3 \times 10^{-3}$ km and $\tilde{\sigma} = 0.7 \times 10^{-3}$ km/s.

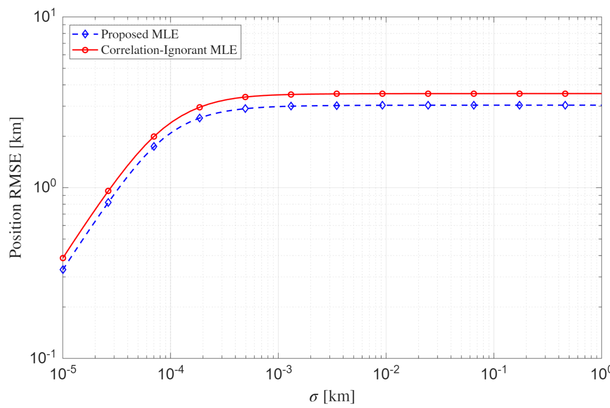

Fig. 11. RMSE of proposed MLE and correlation-ignorant MLE versus the standard deviation of the pseudorange-rate measurement noise ($\tilde{\sigma}$) when $\sigma = 1.3 \times 10^{-3}$ km and $\bar{\gamma} = 0.5$.

correlation-ignorant MLE versus pseudorange noise level σ when $\tilde{\sigma} = 0.7 \times 10^{-3}$ km/s and $\bar{\gamma} = 0.5$. It is noted that the proposed MLE achieves lower RMSE values than the correlation-ignorant MLE over the considered noise range. The improvement is due to the fact that the proposed MLE better matches the true noise statistics. When the noise components in the pseudorange and Doppler measurements are correlated, ignoring this dependence results in non-optimal weighting of the residuals. Using the full covariance matrix allows the proposed MLE to account for this dependence and improves the positioning accuracy. In Fig. 11, the proposed MLE is compared against the correlation-ignorant MLE versus the pseudorange-rate noise level, $\tilde{\sigma}$, when the pseudorange noise level is fixed at $\sigma = 1.3 \times 10^{-3}$ km and $\bar{\gamma} = 0.5$. Similarly, the proposed MLE achieves lower RMSE values over the considered range since it uses the full covariance matrix and accounts for the dependence between the pseudorange and Doppler measurement errors. As $\tilde{\sigma}$ increases, both estimators exhibit a similar saturation behavior, indicating that the Doppler measurements become less informative at high noise levels. However, the proposed MLE remains more accurate.

In Fig. 12, the positioning performance of the proposed MLE and the correlation-ignorant MLE is investigated with respect to $\bar{\gamma}$ when pseudorange and pseudorange-rate noise levels are fixed at $\sigma = 1.3 \times 10^{-3}$ km and $\tilde{\sigma} = 0.7 \times 10^{-3}$ km/s, respectively.

It is observed that the proposed MLE achieves lower RMSE values than the correlation-ignorant MLE when there exists correlation between measurements. This result demonstrates that accurately incorporating the correlation structure allows the estimator to fully exploit the available measurement information, whereas neglecting this correlation consistently degrades the estimation performance. Moreover, the performance gap increases as the magnitude of $\bar{\gamma}$ becomes larger, which indicates that the proposed MLE becomes more advantageous when the measurement noise components are highly correlated. The results further indicate that the estimation performance is nearly symmetric for positive and negative values of $\bar{\gamma}$, suggesting that the positioning accuracy is governed primarily by the magnitude of the measurement correlation rather than by its sign.

Finally, the computational efficiency of the considered MLE-based positioning methods is evaluated in terms of the average runtime required to obtain a single position estimate. The comparison includes the pseudorange-only MLE, the Doppler-only MLE, and the proposed MLE. For the runtime analysis, the receiver-orbital plane angle ϕ is set to $10°$, the sampling period is set to $T = 10$ s, and the noise standard deviations are swept over 60 logarithmically equally spaced values from 10^{-5} to 1. Each estimator is evaluated over five independent realizations with different initial receiver-position offsets and different measurement-noise realizations. For a fair comparison, in each realization, the same initial offsets and the same noise realizations are used for the Doppler-only MLE, the pseudorange-only MLE, and the proposed MLE. For each realization, the same number of estimates is computed for all methods, namely 60 noise levels and 300 Monte Carlo trials per noise level. Hence, the runtime per estimate is obtained by dividing the total elapsed

TABLE I
Average runtime analysis for different MLE based algorithms.

Positioning algorithm	Runtime per estimate [ms]
Pseudorange-only MLE	1.70
Doppler-only MLE	2.62
Proposed MLE	3.32

time by $5 \times 60 \times 300$. The reported runtime includes both the initial three-dimensional grid search stage and the Levenberg-Marquardt optimization. The simulations are performed in MATLAB R2025b on a Windows 11 computer equipped with an Intel Core i9-14900HX processor and 32 GB RAM. The results presented in Table I reveal that the pseudorange-only MLE has the lowest computational time, followed by the Doppler-only MLE, while the proposed MLE has the highest average runtime among the three approaches. Nevertheless, the average runtime of the proposed MLE remains close to those of the traditional approaches. This indicates that the proposed method can jointly exploit pseudorange and Doppler measurements with only a moderate increase in computational time.

V. Extension: Unknown Satellite State at Transmission Time

In this section, we extend the analysis in the previous sections to another scenario in which the satellite state (position, velocity, and clock parameters) is known only at the reception times t_k's, while the signal is actually transmitted at the transmission time instants $t_{k'} = t_k - \delta t_{\rm TOF}(k)$, with $\delta t_{\rm TOF}(k)$ denoting the time of flight related to the kth time instant, as introduced at the beginning of Section II. This scenario becomes more applicable when the satellite state is determined based on various estimation approaches [18], [20], or analytical and machine-learning satellite tracking approaches [18], [21], [46].

The position and the velocity of the satellite at time $t_{k'}$, denoted by $\boldsymbol{r}_{\rm leo}(k')$ and $\dot{\boldsymbol{r}}_{\rm leo}(k')$, respectively, can approximately be stated in terms of the position $\boldsymbol{r}_{\rm leo}(k)$ and the velocity $\dot{\boldsymbol{r}}_{\rm leo}(k)$ of the satellite at time t_k as

$$\boldsymbol{r}_{\rm leo}(k') \approx \boldsymbol{r}_{\rm leo}(k) - \dot{\boldsymbol{r}}_{\rm leo}(k)\,\delta t_{\rm TOF}(k), \tag{66}$$
$$\dot{\boldsymbol{r}}_{\rm leo}(k') \approx \dot{\boldsymbol{r}}_{\rm leo}(k), \tag{67}$$

by assuming constant velocity over short time intervals (on the order of a few milliseconds). Then, the following relation is obtained:

$$\left\| \boldsymbol{r}_{\rm rx} - \big(\boldsymbol{r}_{\rm leo}(k) - \dot{\boldsymbol{r}}_{\rm leo}(k)\,\delta t_{\rm TOF}(k)\big) \right\| = c\,\delta t_{\rm TOF}(k). \tag{68}$$

By taking the square of both sides in (68), solving the quadratic equation in terms of $\delta t_{\rm TOF}(k)$, and choosing the positive root yields

$$\delta t_{\rm TOF}(k) = \frac{1}{c^2 - \|\dot{\boldsymbol{r}}_{\rm leo}(k)\|^2}\Bigg((\boldsymbol{r}_{\rm rx} - \boldsymbol{r}_{\rm leo}(k))^T \dot{\boldsymbol{r}}_{\rm leo}(k) + \bigg[\Big((\boldsymbol{r}_{\rm rx} - \boldsymbol{r}_{\rm leo}(k))^T \dot{\boldsymbol{r}}_{\rm leo}(k)\Big)^2 + (c^2 - \|\dot{\boldsymbol{r}}_{\rm leo}(k)\|^2)\|\boldsymbol{r}_{\rm rx} - \boldsymbol{r}_{\rm leo}(k)\|^2\bigg]^{1/2}\Bigg). \tag{69}$$

Hence, the time-of-flight parameter can be calculated from (69) based on the state of the satellite at time index k for a given position $\boldsymbol{r}_{\rm rx}$ of the receiver. Accordingly, the position of the satellite at time index k' (i.e., at transmission time) can be obtained from (66), which can then be used in (6) and (7) for modeling the measurements.

For the bias and drift parameters of the satellite at transmission times, namely, $\delta t_{\rm leo}(k')$ and $\dot{\delta t}_{\rm leo}(k')$, in (6) and (7), we can consider a constant clock drift over short time intervals; i.e., $\dot{\delta t}_{\rm leo}(k') \approx \dot{\delta t}_{\rm leo}(k)$, and model the bias at transmission time as

$$\delta t_{\rm leo}(k') \approx \delta t_{\rm leo}(k) - \delta t_{\rm TOF}(k)\dot{\delta t}_{\rm leo}(k) \tag{70}$$

Then, based on the time-of-flight expression in (69), we can evaluate (70) for a given receiver position.

Overall, given the states of the satellite at time instants t_k, its states at transmission times $t_{k'}$ can be evaluated as described above, and can be used in the measurements given by (6) and (7). Based on this update, the MLE in Lemma 1 and the CRLB in Lemma 2 can be modified as follows: The definitions of $f_k(\boldsymbol{r}_{\rm rx})$ in (24) and $g_k(\boldsymbol{r}_{\rm rx})$ in (25) are updated as

$$f_k(\boldsymbol{r}_{\rm rx}) \triangleq \rho(k) - \|\boldsymbol{r}_{\rm rx} - \boldsymbol{r}_{\rm leo}(k) + \dot{\boldsymbol{r}}_{\rm leo}(k)\,\delta t_{\rm TOF}(k)\| + c\big(\delta t_{\rm leo}(k) - \delta t_{\rm TOF}(k)\dot{\delta t}_{\rm leo}(k)\big), \tag{71}$$

$$g_k(\boldsymbol{r}_{\rm rx}) \triangleq \dot{\rho}(k) + \frac{\dot{\boldsymbol{r}}_{\rm leo}(k)^T(\boldsymbol{r}_{\rm rx} - \boldsymbol{r}_{\rm leo}(k) + \dot{\boldsymbol{r}}_{\rm leo}(k)\,\delta t_{\rm TOF}(k))}{\|\boldsymbol{r}_{\rm rx} - \boldsymbol{r}_{\rm leo}(k) + \dot{\boldsymbol{r}}_{\rm leo}(k)\,\delta t_{\rm TOF}(k)\|} + c\,\dot{\delta t}_{\rm leo}(k), \tag{72}$$

where $\delta t_{\rm TOF}(k)$ is a function of $\boldsymbol{r}_{\rm rx}$ as specified in (69). Then, the MLE in Lemma 1 can be implemented in the same manner by updating the definitions of $f_k(\boldsymbol{r}_{\rm rx})$ and $g_k(\boldsymbol{r}_{\rm rx})$ as in (71) and (72). For the CRLB calculation in Lemma 2, the only required update is related to the partial derivative expressions in (43) and (44). Since the definitions of $f_k(\boldsymbol{r}_{\rm rx})$ and $g_k(\boldsymbol{r}_{\rm rx})$ are modified as in (71) and (72), the partial derivatives should be calculated based on these expressions, together with the expression in (69). (Those partial derivatives are calculated in Appendix A.) Then, the rest of Lemma 2 remains the same.

VI. Conclusion

In this manuscript, we performed an estimation theoretic analysis for positioning a stationary ground receiver via a single LEO satellite. The MLE and the corresponding CRLB were explicitly derived based on both pseudorange and Doppler measurements, which can contain correlated noise components in given time epochs.

Numerical simulations were performed for positioning error analysis considering various system parameters such as noise level, sampling time, receiver-orbital plane angle and correlation. Furthermore, the proposed methodology was extended to scenarios in which the satellite state is known only at reception times by modeling the propagation delay effect through a time of flight formulation.

Overall, the obtained results demonstrate that accurate positioning with a single LEO satellite is feasible when joint pseudorange and Doppler measurements are considered within an optimal estimation framework in the ML sense. The proposed analysis provides theoretical understanding and practical performance benchmarks for single LEO-based positioning.

A limitation of the present study is that all measurements are generated through simulations. In particular, the same epoch correlation between pseudorange and pseudorange-rate is imposed as a model parameter rather than estimated from real LEO signals. Moreover, the satellite states, including its position, velocity, clock bias, and clock drift, are assumed to be accurately known, and possible mismatches between the true and assumed satellite parameters are not incorporated into the current estimation model. Therefore, the numerical results quantify the effect of an assumed and correctly known measurement correlation structure under ideal satellite state information, but do not experimentally validate the magnitude, sign, stationarity, or receiver and signal-dependent characteristics of the correlation. Future work will focus on incorporating satellite state uncertainties through a misspecified estimation framework and analyzing the effects of satellite-parameter inaccuracies using the misspecified Cramér–Rao bound (MCRB), extending the proposed framework to dynamic receivers, and experimentally validating the proposed approach and its benchmark comparisons using real LEO signal measurements.

Appendix

A. Partial derivatives of (71) and (72)

To obtain a compact expression, we first define

$$\boldsymbol{\Delta r}_k \triangleq \boldsymbol{r}_{\mathrm{rx}} - \boldsymbol{r}_{\mathrm{leo}}(k), \tag{73}$$

$$\eta_k \triangleq c^2 - \|\dot{\boldsymbol{r}}_{\mathrm{leo}}(k)\|^2, \tag{74}$$

$$\zeta_k \triangleq \boldsymbol{\Delta r}_k^T \dot{\boldsymbol{r}}_{\mathrm{leo}}(k), \tag{75}$$

$$\phi_k \triangleq \sqrt{\zeta_k^2 + \eta_k \|\boldsymbol{\Delta r}_k\|^2}\,, \tag{76}$$

and express the time of flight in (69) as

$$\delta t_{\mathrm{TOF}}(k) = \frac{\zeta_k + \phi_k}{\eta_k}\,. \tag{77}$$

In addition, we let

$$\boldsymbol{X}_k \triangleq \boldsymbol{\Delta r}_k + \dot{\boldsymbol{r}}_{\mathrm{leo}}(k)\,\delta t_{\mathrm{TOF}}(k), \quad \boldsymbol{u}_k \triangleq \frac{\boldsymbol{X}_k}{\|\boldsymbol{X}_k\|}.$$

and express the lth components as

$$\Delta r_{k,l} \triangleq r^l_{\mathrm{rx}} - r^l_{\mathrm{leo}}(k), \quad X_{k,l} \triangleq [\boldsymbol{X}_k]_l, \quad u_{k,l} \triangleq [\boldsymbol{u}_k]_l,$$

with $r^l_{\mathrm{leo}}(k)$ denoting the lth component of $\boldsymbol{r}_{\mathrm{leo}}(k)$. Then, based on (77), we obtain

$$\frac{\partial\, \delta t_{\mathrm{TOF}}(k)}{\partial r^l_{\mathrm{rx}}} = \frac{1}{\eta_k}\left(\dot{r}^l_{\mathrm{leo}}(k) + \frac{\zeta_k\, \dot{r}^l_{\mathrm{leo}}(k) + \eta_k\, \Delta r_{k,l}}{\phi_k}\right). \tag{78}$$

for $l \in \{1,2,3\}$, where $\dot{r}^l_{\mathrm{leo}}(k)$ represents the lth component of $\dot{\boldsymbol{r}}_{\mathrm{leo}}(k)$.

We can re-write (71) and (72) in terms of the definitions above as

$$f_k(\boldsymbol{r}_{\mathrm{rx}}) = \rho(k) - \|\boldsymbol{X}_k\| + c\big(\delta t_{\mathrm{leo}}(k) - \delta t_{\mathrm{TOF}}(k)\, \dot{\delta t}_{\mathrm{leo}}(k)\big)\,, \tag{79}$$

$$g_k(\boldsymbol{r}_{\mathrm{rx}}) = \dot{\rho}(k) + \frac{\dot{\boldsymbol{r}}_{\mathrm{leo}}(k)^T \boldsymbol{X}_k}{\|\boldsymbol{X}_k\|} + c\, \dot{\delta t}_{\mathrm{leo}}(k). \tag{80}$$

Then, the partial derivatives w.r.t. r^l_{rx} are obtained as

$$\frac{\partial f_k(\boldsymbol{r}_{\mathrm{rx}})}{\partial r^l_{\mathrm{rx}}} = -\, u_{k,l} \;-\; \Big(\boldsymbol{u}_k^T \dot{\boldsymbol{r}}_{\mathrm{leo}}(k) + c\, \dot{\delta t}_{\mathrm{leo}}(k)\Big)\, \frac{\partial\, \delta t_{\mathrm{TOF}}(k)}{\partial r^l_{\mathrm{rx}}}, \tag{81}$$

$$\begin{aligned}\frac{\partial g_k(\boldsymbol{r}_{\mathrm{rx}})}{\partial r^l_{\mathrm{rx}}} &= \frac{\dot{r}^l_{\mathrm{leo}}(k) - \big(\boldsymbol{u}_k^T \dot{\boldsymbol{r}}_{\mathrm{leo}}(k)\big)\, u_{k,l}}{\|\boldsymbol{X}_k\|} \\ &\quad + \frac{\|\dot{\boldsymbol{r}}_{\mathrm{leo}}(k)\|^2 - \big(\boldsymbol{u}_k^T \dot{\boldsymbol{r}}_{\mathrm{leo}}(k)\big)^2}{\|\boldsymbol{X}_k\|}\, \frac{\partial\, \delta t_{\mathrm{TOF}}(k)}{\partial r^l_{\mathrm{rx}}},\end{aligned} \tag{82}$$

which can be evaluated via (78). $\square$

Acknowledgment

Google Gemini was used during the literature survey for generating the BibTex entries of the papers in the literature.

References

[1] M. Jiang et al., "LEO Doppler-aided GNSS position estimation," *GPS Solutions*, vol. 26, no. 31, 2022.

[2] I. Shayea et al., "Integration of 5G, 6G and IoT with low Earth orbit (LEO) networks: Opportunity, challenges and future trends," *Results in Engineering*, vol. 23, p. 102409, 2024.

[3] Y. Liao, S. Liu, X. Hong, J. Shi, and L. Cheng, "Integration of communication and navigation technologies toward LEO-enabled 6G networks: A survey," *Space: Science & Technology*, vol. 3, 2023, Art. no. 0092.

[4] D.-R. Emenonye, H. S. Dhillon, and R. Michael Buehrer, "Fundamentals of LEO-based localization," *IEEE Transactions on Information Theory*, vol. 71, no. 7, pp. 5277–5311, 2025.

[5] M. Hui, S. Zhai, D. Wang, T. Hui, W. Wang, P. Du, and F. Gong, "A review of LEO-satellite communication payloads for integrated communication, navigation, and remote sensing: Opportunities, challenges, future directions," *IEEE Internet of Things Journal*, vol. 12, no. 12, pp. 18 954–18 992, 2025.

[6] J. He, S. Ni, H. Lin, Z. Liu, and Z. Xiao, "Survey on positioning technology based on signal of opportunity from low earth orbit," *Frontiers in Physics*, vol. 13, 2025.

[7] J. J. Khalife and Z. M. Kassas, "Receiver design for Doppler positioning with LEO satellites," in *2019 IEEE International Conference on Acoustics, Speech and Signal Processing (ICASSP)*, 2019, pp. 5506–5510.

[8] Y. Meng, L. Bian, L. Han, W. Lei, T. Yan, M. He, and X. Li, "A global navigation augmentation system based on LEO communication constellation," in *2018 European Navigation Conference (ENC)*, 2018, pp. 65–71.

[9] R. Sabbagh and Z. M. Kassas, "Observability analysis of receiver localization via pseudorange measurements from a single LEO satellite," *IEEE Control Systems Letters*, vol. 7, pp. 571–576, 2023.

[10] ——, "Observability analysis of opportunistic receiver localization with LEO satellite pseudorange measurements," in *35th International Technical Meeting of the Satellite Division of the Institute of Navigation*, Sep. 2022, pp. 1890–1901.

[11] Y. Xu et al., "Joint pseudo-range and Doppler positioning method with LEO satellite signals of opportunity," *Satellite Navigation*, vol. 6, no. 1, p. 10, 2025.

[12] K. Udofia, "Determination of visibility time of LEO and MEO satellites with circular orbits," *Journal of Multidisciplinary Engineering Science and Research (JMESR)*, vol. 1, no. 3, pp. 188–193, Sep. 2022.

[13] N. Jardak, R. Adam, and Q. Jault, "Leveraging multi-LEO satellite signals for opportunistic positioning," *IEEE Access*, vol. 12, pp. 127 100–127 114, 2024.

[14] Z. M. Kassas et al., "Navigation with multi-constellation LEO satellite signals of opportunity: Starlink, OneWeb, Orbcomm, and Iridium," in *2023 IEEE/ION Position, Location and Navigation Symposium*, 2023, pp. 338–343.

[15] S. E. Kozhaya and Z. M. Kassas, "Positioning with starlink LEO satellites: A blind Doppler spectral approach," in *2023 IEEE 97th Vehicular Technology Conference*, 2023, pp. 1–5.

[16] H. More, E. Cianca, and M. De Sanctis, "Comparing positioning performance of LEO mega-constellations and GNSS in urban canyons," *IEEE Access*, vol. 12, pp. 24 465–24 482, 2024.

[17] N. Khairallah and Z. M. Kassas, "Ephemeris tracking and error propagation analysis of LEO satellites with application to opportunistic navigation," *IEEE Transactions on Aerospace and Electronic Systems*, vol. 60, no. 2, pp. 1242–1259, 2024.

[18] ——, "Ephemeris closed-loop tracking of LEO satellites with pseudorange and Doppler measurements," in *34th International Technical Meeting of the Satellite Division of the Institute of Navigation*, Sep. 2021, pp. 2544–2555.

[19] J. Ma, P. Zheng, X. Liu, Y. Zhang, A. A. Nasir, and T. Y. Al-Naffouri, "Positioning using LEO satellite communication signals under orbital errors," 2025. [Online]. Available: https://arxiv.org/abs/2511.06060

[20] J. Khalife, M. Neinavaie, and Z. M. Kassas, "Navigation with differential carrier phase measurements from megaconstellation LEO satellites," in *IEEE/ION Position, Location and Navigation Symposium*, 2020, pp. 1393–1404.

[21] J. Haidar-Ahmad, N. Khairallah, and Z. M. Kassas, "A hybrid analytical-machine learning approach for LEO satellite orbit prediction," in *25th International Conference on Information Fusion (FUSION)*, 2022, pp. 1–7.

[22] S. Hayek and Z. M. Kassas, "Modeling and compensation of timing and spatial ephemeris errors of non-cooperative LEO satellites with application to PNT," *IEEE Transactions on Aerospace and Electronic Systems*, vol. 61, no. 3, pp. 5579–5593, 2025.

[23] N. Jardak and Q. Jault, "The potential of LEO satellite-based opportunistic navigation for high dynamic applications," *Sensors*, vol. 22, no. 7, 2022, Art. no. 2541.

[24] D.-R. Emenonye, H. S. Dhillon, and R. M. Buehrer, "3D positioning with unsynchronized LEO satellites and minimal infrastructure," in *IEEE 100th Vehicular Technology Conference*, 2024, pp. 1–7.

[25] G. Yao, Z. Huang, H. Zhou, and X. Zhang, "Single satellite positioning method and error characteristic analysis of LEO navigation satellites," in *China Satellite Navigation Conference*, ser. Lecture Notes in Electrical Engineering, C. Yang and J. Xie, Eds., 2024, vol. 1093, pp. 28–39.

[26] S. Shahcheraghi, F. N. Gourabi, M. Neinavaie, and Z. M. Kassas, "Joint doppler and azimuth doa tracking for positioning with iridium leo satellites," in *Proceedings of the 36th International Technical Meeting of the Satellite Division of the Institute of Navigation (ION GNSS+ 2023)*, Denver, Colorado, September 2023, pp. 2373–2383.

[27] Z. M. Kassas, N. Khairallah, and S. Kozhaya, "Ad Astra: simultaneous tracking and navigation with megaconstellation LEO satellites," *IEEE Aerospace and Electronic Systems Magazine*, vol. 39, no. 9, pp. 46–71, 2024.

[28] S. Shahcheraghi, J. Saroufim, and Z. M. Kassas, "Acquisition, doppler tracking, and differential LEO-aided IMU navigation with uncooperative satellites," *IEEE Aerospace and Electronic Systems Magazine*, vol. 40, no. 5, pp. 54–72, 2025.

[29] J. J. Morales, P. F. Roysdon, and Z. M. Kassas, "Signals of opportunity aided inertial navigation," in *29th International Technical Meeting of the Satellite Division of the Institute of Navigation*, Sep. 2016, pp. 1492–1501.

[30] J. J. Morales, J. Khalife, A. A. Abdallah, C. T. Ardito, and Z. M. Kassas, "Inertial navigation system aiding with Orbcomm LEO satellite Doppler measurements," in *31st International Technical Meeting of the Satellite Division of the Institute of Navigation*, Miami, Florida, Sep. 2018, pp. 2718–2725.

[31] M. Leng et al., "Anchor-aided joint localization and synchronization using SOOP: Theory and experiments," *IEEE Transactions on Wireless Communications*, vol. 15, no. 11, pp. 7670–7685, 2016.

[32] W.-H. Hsu and S.-S. Jan, "Assessment of using doppler shift of leo satellites to aid gps positioning," in *2014 IEEE/ION Position, Location and Navigation Symposium*, 2014, pp. 1155–1161.

[33] L. Li, J. Zhong, and M. Zhao, "Doppler-aided GNSS position estimation with weighted least squares," *IEEE Transactions on Vehicular Technology*, vol. 60, no. 8, pp. 3615–3624, Oct. 2011.

[34] H. Ge et al., "LEO enhanced global navigation satellite system (LeGNSS): Progress, opportunities, and challenges," *Geospatial Information Science*, vol. 25, no. 1, pp. 1–13, 2022.

[35] L. Wang et al., "Initial assessment of the LEO based navigation signal augmentation system from Luojia-1A satellite," *Sensors*, vol. 18, no. 11, 2018, Art. no. 3919.

[36] Z. Tan, H. Qin, L. Cong, and C. Zhao, "Positioning using IRIDIUM satellite signals of opportunity in weak signal environment," *Electronics*, vol. 9, no. 1, 2020, Art. no. 37.

[37] J. Li, C. Han, N. Ye, J. Pan, K. Yang, and J. An, "Instant positioning by single satellite: Delay-doppler analysis method enhanced by beam-hopping," *IEEE Transactions on Vehicular Technology*, vol. 74, no. 9, pp. 14 418–14 430, 2025.

[38] W. G. Melbourne et al., "The application of spaceborne GPS to atmospheric limb sounding and global change monitoring," Jet Propulsion Laboratory, California Institute of Technology, Pasadena, California, Tech. Rep. JPL Publication 94-18, Apr. 1994.

[39] Z. Z. M. Kassas, *Navigation from Low Earth Orbit: Part 2: Models, implementation, and performance*. John Wiley & Sons, Ltd, 2021, ch. 43, pp. 1381–1412.

[40] M. R. Gholami, S. Gezici, and E. G. Strom, "TDOA based positioning in the presence of unknown clock skew," *IEEE Transactions on Communications*, vol. 61, no. 6, pp. 2522–2534, 2013.

[41] S. Fortunati et al., "Performance bounds for parameter estimation under misspecified models: Fundamental findings and applications," *IEEE Signal Processing Magazine*, vol. 34, no. 6, pp. 142–157, 2017.

[42] S. Fortunati, F. Gini, and M. S. Greco, "Chapter 4 - Parameter bounds under misspecified models for adaptive radar detection," in *Academic Press Library in Signal Processing, Volume 7*, R. Chellappa and S. Theodoridis, Eds. Academic Press, 2018, pp. 197–252.

[43] F. Roemer, "Misspecified Cramer-Rao bound for delay estimation with a mismatched waveform: A case study," in *IEEE International Conference on Acoustics, Speech and Signal Processing*, 2020, pp. 5994–5998.

[44] H. V. Poor, *An Introduction to Signal Detection and Estimation*, 2nd ed. New York, NY, USA: Springer, 1994.

[45] J. J. Morales, J. Khalife, U. S. Cruz, and Z. M. Kassas, "Orbit modeling for simultaneous tracking and navigation using LEO satellite signals," in *32nd International Technical Meeting of the Satellite Division of the Institute of Navigation*, Miami, Florida, Sep. 2019, pp. 2090–2099.

[46] D. Shen et al., "Methods of machine learning for space object pattern classification," in *2019 IEEE National Aerospace and Electronics Conference (NAECON)*, 2019, pp. 565–572.